SANDIA REPORT

SAND2011-3737
Unlimited Release
Printed June 2011

Ground Water and Snow Sensor Based on Directional Detection of Cosmogenic Neutrons

Robert L. Cooper, Patrick Griffin, and Peter Marleau

Prepared by
Sandia National Laboratories
Albuquerque, New Mexico 87185 and Livermore, California 94550

Sandia National Laboratories is a multi-program laboratory managed and operated by Sandia Corporation, a wholly owned subsidiary of Lockheed Martin Corporation, for the U.S. Department of Energy's National Nuclear Security Administration under contract DE-AC04-94AL85000.

Sandia National Laboratories

Issued by Sandia National Laboratories, operated for the United States Department of Energy by Sandia Corporation.

Printed in the United States of America. This report has been reproduced directly from the best available copy.

Available to DOE and DOE contractors from
U.S. Department of Energy
Office of Scientific and Technical Information
P.O. Box 62
Oak Ridge, TN 37831

Telephone: (865) 576-8401
Facsimile: (865) 576-5728
E-Mail: reports@adonis.osti.gov
Online ordering: http://www.osti.gov/bridge

Available to the public from
U.S. Department of Commerce
National Technical Information Service
5285 Port Royal Rd.
Springfield, VA 22161

Telephone: (800) 553-6847
Facsimile: (703) 605-6900
E-Mail: orders@ntis.fedworld.gov
Online order: http://www.ntis.gov/help/ordermethods.asp?loc=7-4-0#online

SAND2011-3737
Unlimited Release
Printed June 2011

Ground Water and Snow Sensor Based on Directional Detection of Cosmogenic Neutrons

Robert Cooper and Peter Marleau
Rad/Nuc Detection Systems
Sandia National Laboratories
P.O. Box 969
Livermore, California 94551-MS9406

Patrick Griffin
Applied Nuclear Technologies
Sandia National Laboratories
P.O. Box 5800
Albuquerque, New Mexico 87185-MS1146

Abstract

A fast neutron detector is being developed to measure the cosmic ray neutron flux in order to measure soil moisture. Soil that is saturated with water has an enhanced ability to moderate fast neutrons, removing them from the backscatter spectrum. The detector is a two-element, liquid scintillator detector. The choice of liquid scintillator allows rejection of gamma background contamination from the desired neutron signal. This enhances the ability to reconstruct the energy and direction of a coincident neutron event. The ability to image on an event-by-event basis allows the detector to selectively scan the neutron flux as a function of distance from the detector. Calibrations, simulations, and optimization have been completed to understand the detector response to neutron sources at variable distances and directions. This has been applied to laboratory background measurements in preparation for outdoor field tests.

ACKNOWLEDGMENTS

We would like to acknowledge the 8132 group for all their support, encouragement, and technical advice throughout the project. Specifically, we would like to thank James Lund and Nick Mascarenhas for a wealth of initial advice and advising to build this project. Thanks go to John Steele and Stanley Mrowka for assistance in developing and building the DAQ system. James Brennan and Dan Throckmorton deserve thanks for the skilled job in assembling and machining much of the detector. R.C. would like to acknowledge the early career LDRD program that made this project possible.

CONTENTS

FIGURES

TABLES

NOMENCLATURE

ADC	Analog-to-Digital Converter
AmBe	A neutron source material from the combination of ^{241}Am+Be
COSMOS	Cosmic-Ray Soil Moisture Observing System
DAQ	Data Acquisition System
ENDF	Evaluated Nuclear Data Files
GeV	Billion electron-volts
HDPE	High-density polyethylene
ISO	International Organization for Standardization
MCNP	Monte Carlo N-Particle
MeV	Million electron-volts
MeVee	MeV electron equivalent
MLEM	Maximum Likelihood Estimation Method
NIM	Nuclear Instrumentation Module
NIST	National Institute of Standards and Technology
NSC	Neutron Scatter Camera
NSF	National Science Foundation
PMT	Photomultiplier Tube
PSD	Pulse shape discrimination
TAC	Time-to-Amplitude Converter
TOF	Time-of-flight
VME	Versa Modula Europa

1. INTRODUCTION

In this report, we summarize the current status of a detector that utilizes the ubiquitous cosmic ray spectrum to measure soil water content. This detector is sensitive to the fast neutron component of the cosmic rays (approximately 1-10 MeV), and the modulation of this spectrum by soil water is the primary source of signal. As will be described below, there is recent work utilizing the thermal neutron component (~0.025 eV) of the cosmic ray spectrum to perform similar studies. We will show that our work is a natural complement to the thermal neutron detection studies, and that a fast neutron detector offers potential benefits not possible with thermal neutron detection. In addition, the design geometry allows directional differentiation that can be used to isolate the various components of neutrons.

As a general outline, the remainder of this section will discuss the importance and current limitations in soil hydrology measurements. Then, the generation of cosmic ray neutrons will be discussed. A brief discussion of the principle of operation of the proposed detector will conclude this section. The next section will describe a modeling program undertaken to understand the soil response to atmospheric cosmic ray neutrons. No attempt is made to be comprehensive as entire fields of study are dedicated to these issues. The goal is to understand the bulk effect water has on the relative neutron signal the detector is sensitive to. The next section will describe the experimental apparatus and its calibration. This section will move beyond the basic principles of operation given at the end of this section. The results of laboratory tests will be summarized in the penultimate section, and finally, concluding remarks are given in the last section. Future work and detector capabilities will be highlighted to motivate continued work in this Investment Area.

1.1. Motivation

Water is an important natural resource, and understanding its ebb and flow is vital to our national security. The national infrastructure depends critically on the seasonal reserve and use of water in all forms. This point is particularly salient in Northern California in the Bay Area. When coupling natural seasonal cycles with long-term climate change, only a program of widespread hydrology measurements can properly inform policy [1]. Currently, satellites in orbit use microwaves to monitor the Earth, but as we shall see, these are inadequate for the deep understanding of hydrology necessary.

The successful monitoring of water over these large swathes of land has a fundamental impact into our understanding of the water cycle as well as being applicable to agriculture, climate change science, etc. It should be noted that this report is most applicable to terrestrial applications, but the same technology could be adapted to extra-terrestrial water searches. In fact, cosmic-ray neutrons were used to measure water content on the surface of Mars [2-4]

The current state of water measurements is a problem of scales. At the scale of approximately a few centimeters, one can assay the soil water content through direct means. To achieve any reasonable estimate of soil water content over a medium range would entail a timely (and potentially costly) series of many local measurements to effectively measure the average water content. Coupling this with the high variability and inhomogeneity of various soil parameters (composition, density, porosity, etc.) this task is daunting [5]. On the other hand, remote sensing with satellites gives hydrological data averaged over many square kilometers. Satellites are limited to areas lacking dense vegetation, and the water depth in the soil can also limit accurate measurement [6]. Therefore, for these reasons, the intermediate scale is the "Holy Grail" of hydrology measurements.

The intermediate scale for hydrology measurements is interesting for a number of reasons. A series of these measurements is considered necessary to accurately calibrate the measurements of remote sensing satellites. The shortcomings of satellites has already been mentioned, but even when satellite measurements are possible, they are generally incapable of differentiating the mechanism that water is trapped by (canopy, snowpack, soil water, etc.). The variability of terrain is obviously dominated by the intermediate scale, and large swath averages are ignorant to important scientific effects [5]

The use of cosmic-ray neutrons to measure water content in this intermediate region is not unprecedented [7-9]. In fact, the NSF has invested over $5M in the ambitious Cosmic-Ray Soil Moisture Observing System (COSMOS) project to develop and install a nationwide network of thermal neutron detectors to for the purpose of hydrology measurements [10]. A popular article in US News and World Report can be found in the references [11].

Finally, the usual detection technology for neutron detectors is ^{3}He. As many popular articles have articulated the world's ^{3}He supply is in short supply. A long-term goal of this project is not only neutron detection, but possibly its field deployment on a massive scale. With this in mind, a viable substitute for ^{3}He is appropriate. Simplicity, ruggedization, and cost should also be considered at some level in this early work. Therefore, many detector concepts can be envisioned that would solve this hydrology problem, but would be prohibitive and impractical to deploy on a large scale.

1.2. Cosmic Ray Neutrons

Astrophysical processes across the galaxy produce high-energy atomic nuclei that get accelerated to high energies over many light years and eventually strike Earth. Figure 1 shows the differential fluxes of various primary cosmic rays versus incident energy, and of these nuclei, about 80% are protons and 14% are alpha particles [12-13]. The van Allen radiation belt and Earth's magnetic field has a strong influence upon the trajectories of these protons. These effects manifest themselves as modulations to cosmic ray spectrum measured on the ground as a function of magnetic lines of latitude.

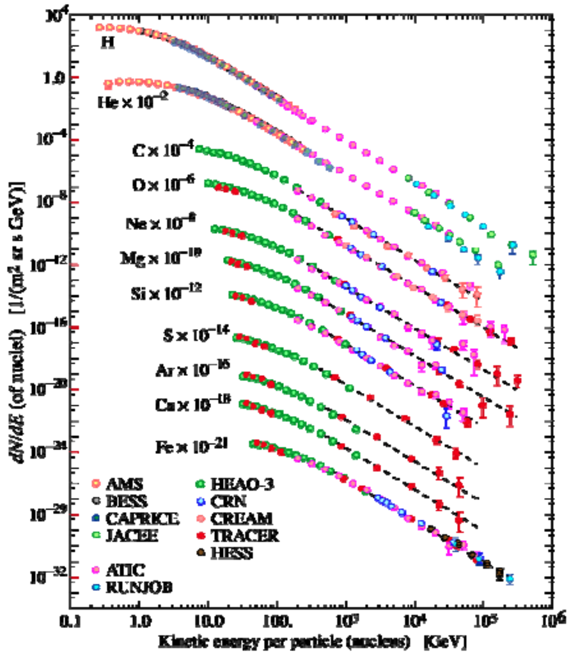

Figure 1: The flux of primary cosmic rays impinging on the upper atmosphere is shown as a function of incident energy. The cosmic ray spectrum is largely high-energy protons. Image taken the Particle Data Group [12].

These protons then impinge upon the upper atmosphere with many GeV of energy, and their collisions with atmospheric nitrogen and oxygen induce strong showers and cascades of other particles such as pions, excited-state nuclei, and high-energy nucleons. These secondary cosmic ray particles can decay, relax to their ground states, etc. into a cascade of muons, neutrinos, neutrons, etc. For purposes of this project, there is a particularly large number of ~1 MeV neutrons are produced from evaporation reactions off the excited nuclei [14]. Figure 2 shows a schematic of this process. Figure 3 shows the relative composition of the cosmic rays as a function of altitude in the atmosphere. While the muons and neutrinos dominate the flux, only the neutrons have a significant interaction in water that the detector can measure. In general, the muons are high energy and continuously lose energy in a more-or-less straight-line path through the Earth. The neutrinos generally don't interact at all.

A more detailed exposition is beyond the scope of this report, but the reader is referred to the references above and reference contained therein. The reference by Ziegler is written with single event faults in computer science in mind, and it is also referred [15].

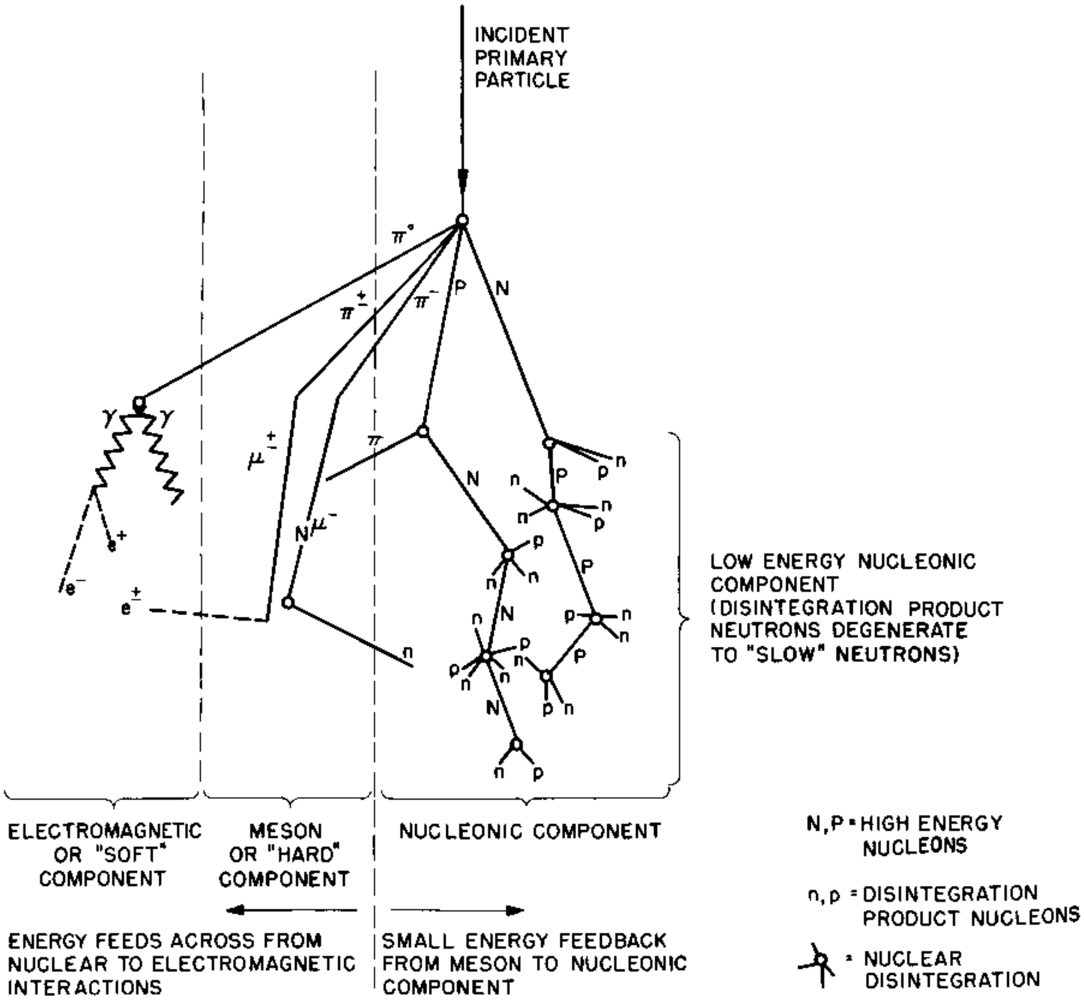

Schematic Diagram of Cosmic Ray Shower

Figure 2: A schematic of a cosmic ray shower is shown. Image taken from http://www.fisica.unlp.edu.ar/~veiga/experiments.html.

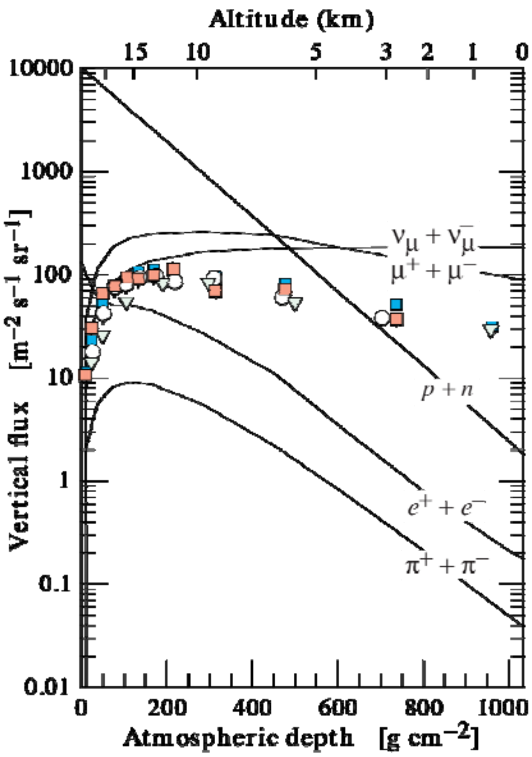

Figure 3: The flux of cosmic ray components is shown as a function of altitude (given in areal density which can be related to atmospheric pressure and altitude). We see that neutrinos and muons are the dominant component, but the neutrons are the species of interest. The data points on the plot are for negatively charged muons. Image taken from the Particle Data Group [12].

1.3. Principle of Operation

As the high-energy flux of neutrons approaches Earth's surface, they scatter and lose energy with the atmosphere and the soil. These scattering collisions can lead to many of the fast neutrons being moderated to thermal temperatures. The interactions result in a mixture of thermal, epithermal, and fast neutrons at the detector. When neutrons enter soil that is saturated with water, the fast neutrons are more effectively moderated to thermal energies because of the elastic collisions of neutrons on the protons (hydrogen nucleus). As is known from nuclear reactor design, protons are exceptional moderators because the proton is nearly the same mass as the neutron. Otherwise, in dry soil, the fast neutrons tend to scatter off the heavier elements, and many of these fast neutrons will be backscattered back towards the atmosphere before fully thermalizing. The presence of the water moderator tends to suppress the backscattering of fast neutrons, and a "puddle" of thermal neutrons is produced.

Sheu *et al*. modeled the response of the cosmic ray neutron spectrum to dry soil and a pure water interface. As expected, the thermal neutron content increases near the interface, and the fast neutron number decreases. These results are shown in a representative plot in figure 4.

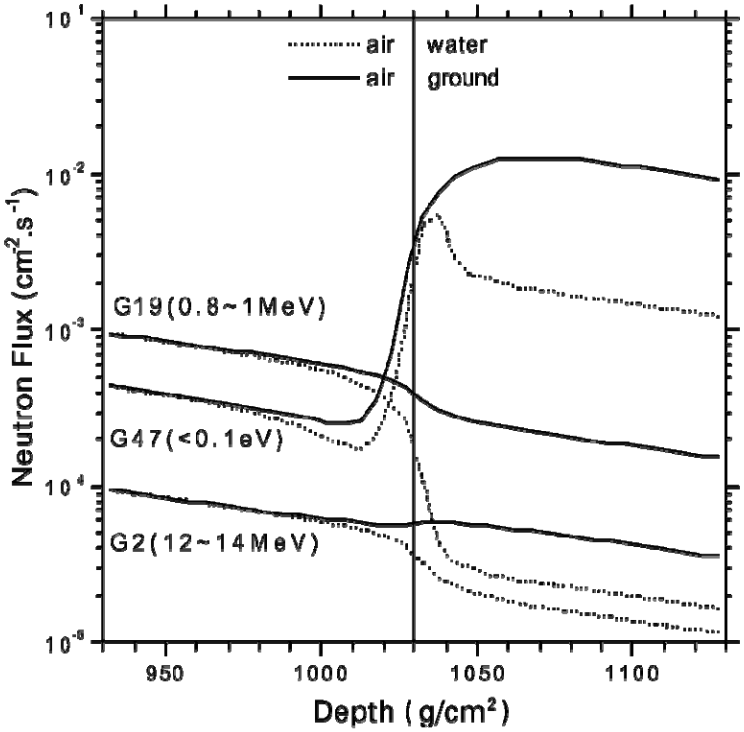

Figure 4: A plot from Sheu *et al*. [16] showing the response of various neutron energy groups to an air-water and air-soil interface. The presence of water is found to modulate the presence of thermal and fast neutrons.

Previous work has been done to monitor the thermal neutron component near the surface as a gauge of the soil water content [7-9]. In these works, the detectors capture thermal neutrons and exothermically disintegrate into charged particles or photons (e.g. $^{10}B(n,\alpha)^{7}Li$ and $^{3}He(n,p)t$ for the works above). The work of Sheu *et al*. [16] considers moderating a BF_3 detector to offer sensitivity to fast neutrons, but a feature common to all these detection method is the lack of energy spectroscopy of the neutrons. Additionally, the neutrons are completely absorbed when they interact, and only singles measurements are possible.

The response of a singles counter type of detector (such as a ^{3}He proportional counter) will fall off as $(\rho^2 + h^2)^{-1}$ where ρ is the ground distance from the detector to the neutron source and h is the detector height off the ground. Despite a neutron source enhancement of $2\pi\rho$ from concentric rings of soil sources, the overall sensitivity will fall as $\sim\rho^{-1}$. This means a counter will be most sensitive to the local area nearest the detector. Figure 5 shows this situation schematically.

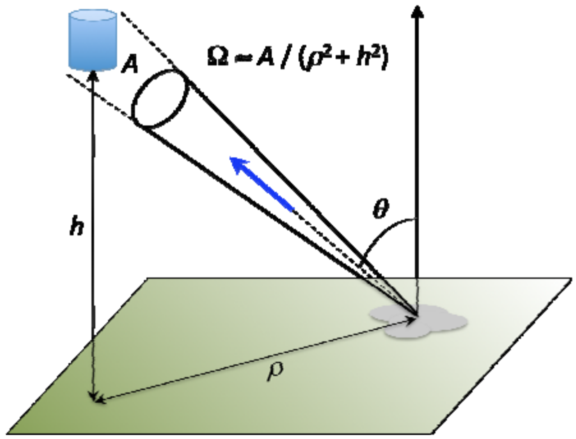

Figure 5: The schematic representation of a single counter detector is shown.

The proposed detector is a two-element, fast neutron detector arranged symmetrically along the vertical axis. It is shown schematically in figure 6. The detector operates in a similar manner to the neutron scatter camera (NSC) in place at Sandia [17-18]. By requiring a coincidence scatter in both detectors, the neutron energy and direction can be reconstructed. This allows a downward traveling neutron from the cosmic spectrum to be differentiated from an upward traveling neutron from the ground. Ideally, the detector could image a neutron source on an event-by-event basis. By requiring multiple interactions, the detector can be "electronically" collimated in order to improve sensitivity to events occurring at larger ρ than a single counter type of detector.

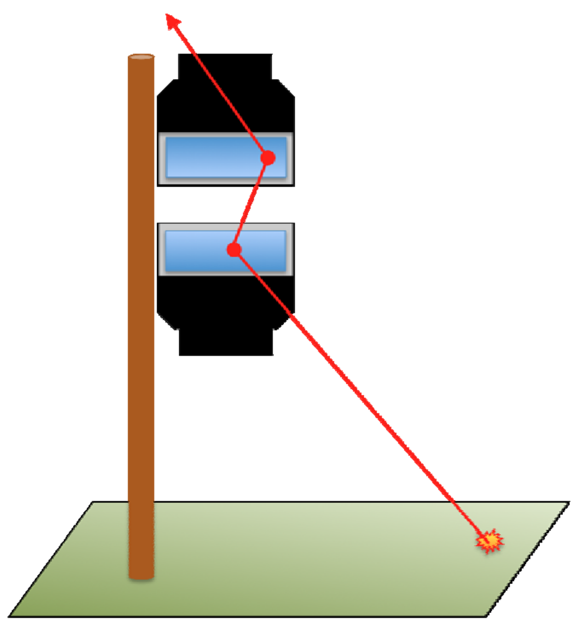

Figure 6: A schematic diagram showing the multi-element neutron detector situated vertically. It can utilize multiple elastic scattering of fast neutrons to infer both the original neutrons energy and direction.

Similar to the NSC, the detector is sensitive to approximately 1-10 MeV neutrons. This is in the fission energy range, and typical laboratory sources for homeland security applications can be used to investigate this detector (just as with the NSC). Despite the similarity to the NSC, this detector operates in a fundamental different mode by requiring high sensitivity and accepting marginal imaging capabilities. Furthermore, simplicity and cost are key features that are needed to large-scale deployment. The optimization of this detector must satisfy almost mutually exclusive criteria from the NSC.

By designing the data acquisition system (DAQ) to trigger on any single interaction and using an offline, software analysis to construct the coincident events, the potential low rate of coincidences can be circumvented. The detector can then operate in both singles and coincident mode simultaneously. The ability to trigger in singles mode allows it to achieve high count-rates, and the ability to reconstruct coincident events allows the detector to image and perform energy spectroscopy on the neutron sources.

2. MODELING SOIL RESPONSE

The discussion below is intended to be a cursory summary of the methods used to examine the neutron output with and without water in the soil. In this treatment, we use a fit to the data by Gordon *et al*. [19]. The formula used is

$$d\phi_0(E)/dE = \sum_{i=1}^{2} c_i \exp\left[-\beta_i(\ln(E))^2 + \gamma_i \ln(E)\right]$$

where the parameters are given in table 1. A plot of both the differential energy spectrum and the integrated counts spectrum is shown in figure 7.

Table 1: Table of coefficients used in the Gordon *et al*. [19] formula described above.

i	β_i	γ_i	c_i
1	0.3500	2.1451	1.006×10^{-6}
2	0.4106	-0.6676	1.011×10^{-3}

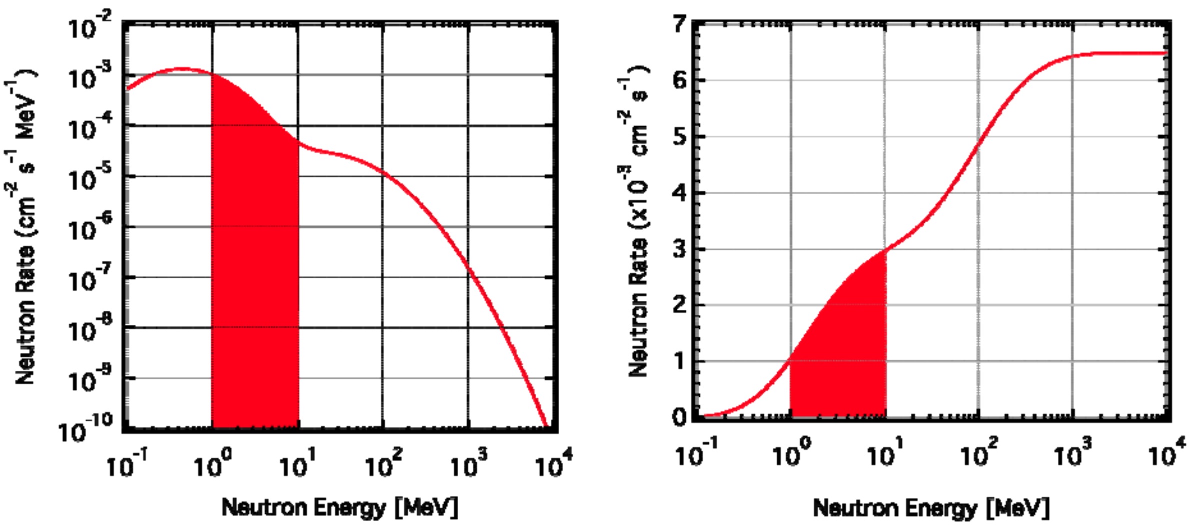

Figure 7: On the left is the differential energy spectrum of cosmic ray neutrons from the fit in Gordon *et al*. [19]. On the right is the integrated spectrum. The shaded area is nominally the detector's energy sensitivity region (1-10 MeV). Within this energy region, the cosmic ray neutron rate is expected to be approximately 2 × 10^{-3} cm^{-2} s^{-1}.

To simulate the soil response, the Gordon parameterization was used to simulate the downward neutron energy flux from the cosmic rays impinging upon the surface. The angular distribution was modeled as a $\cos^2\theta$ distribution with respect to the downward vertical direction as motivated by Ziegler [15]. It is very important to note that this is the solid angle distribution $dN/d\cos\theta$ and not an angle distribution $dN/d\theta$.

The incident neutron distribution was simulated as striking an average soil content with 25% water and 0% water by volume. The bulk soil density ρ_B is a linear combination of a density of dry soil ρ_S and water density ρ_W. It is

$$\rho_B = \rho_S(1-S) + \rho_W S P_V,$$

where S is volume of pores in the soil, and P_V is the fraction of these pores filled with water. Figure 8 illustrates this. Typical values for the density (roughly 2.0 g cm^{-3}) and makeup of the soil are given in [20-21].

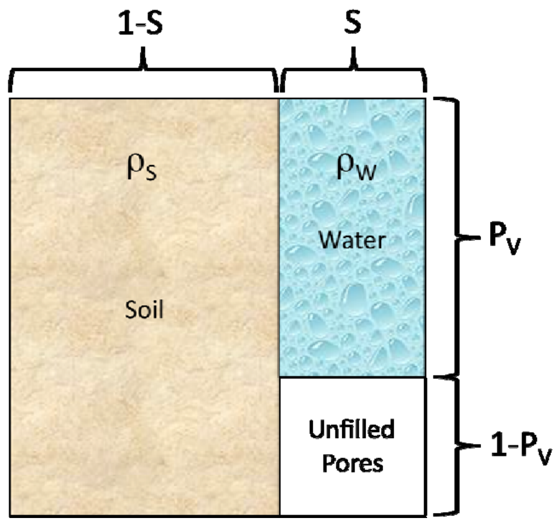

Figure 8: A schematic of the water content used in the simulation is shown.

The simulation package Monte Carlo N-Particle 5 (MCNP5) [22] was used to simulate the neutron transport in the soil, and its ptrac facility was used in an analog simulation to track the backscattered neutrons down to thermal energies. The input spectrum to MCNP5 was the Gordon spectrum from 100 keV to 50 MeV. The 50 MeV cutoff is generally a limitation of the MCNP5 ENDF libraries, and the MCNP-X [23] or the or MCNP-PoliMi [24] package could be used to extend this range. The simulation energy range is well outside the energy sensitivity of the detector to accommodate the possibility of significant down scattering or exothermic, thermal neutron capture reactions.

The simulation was performed at a single point to simplify the tallying of results. In fact, this can be shown to lead to no loss of information if the distance traveled in soil is tabulated and the soil is reasonably homogeneous over the range of travel. The simulations show a marked decrease in the number of neutrons in the 1-5 MeV energy range. In the water saturated soil (25% by volume), the neutron backscatter rate drops to nearly 60% of the dry soil rate for 2 MeV backscattered neutrons. The angular distribution is mostly unchanged, and it is essentially a $dN/d\cos\theta \approx \cos\theta$ distribution. The average emission radius with respect to the entry point is significantly different when the soil is hydrated (this would seem to indicate multiple scattering on the water), but the range is already so small with respect to the scale of the experiment that it can be safely ignored. These results are shown in figure 9.

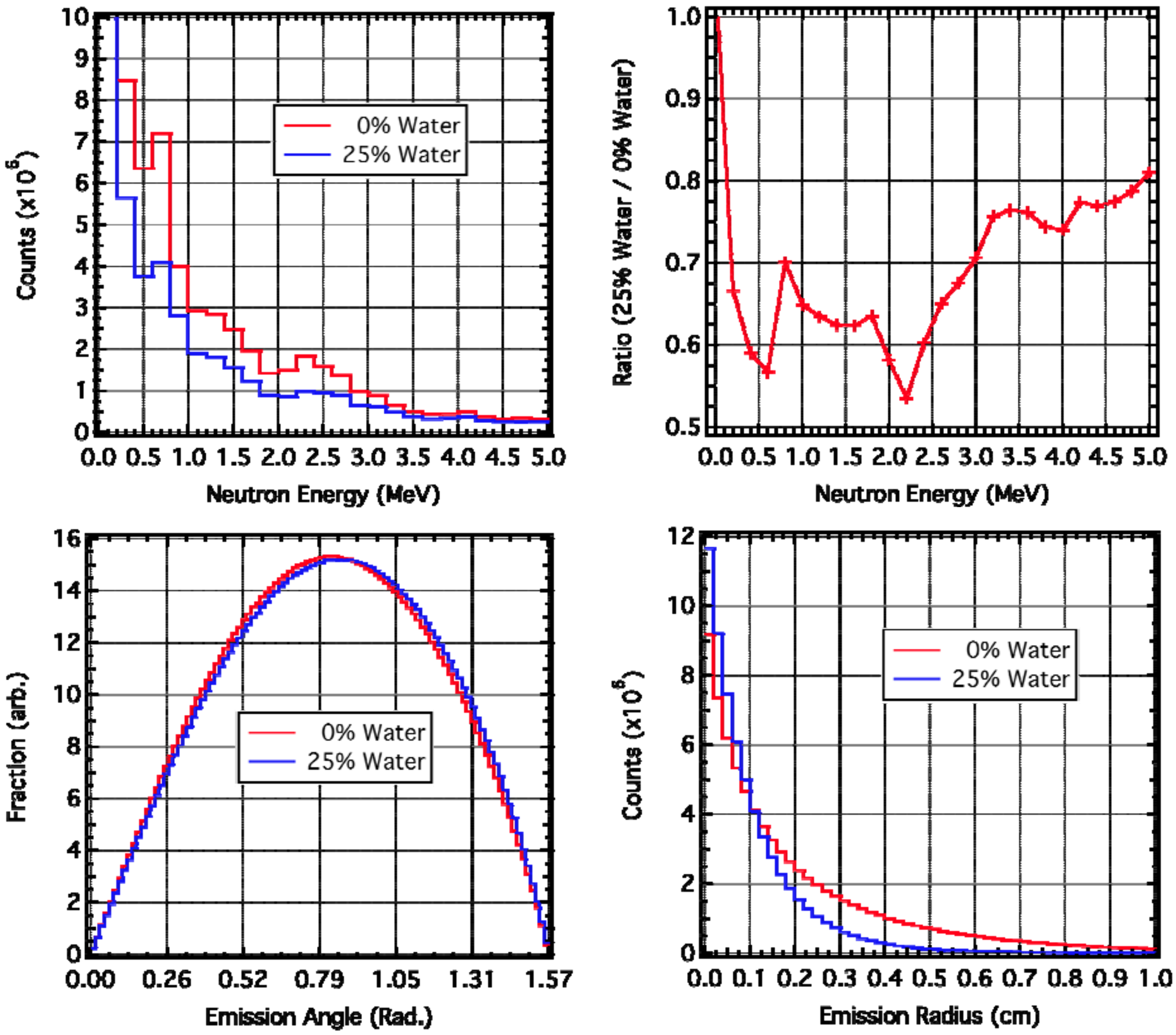

Figure 9: (upper-left) A histogram of the energy output as a function of soil water content is shown. (upper-right) The ratio of the histograms in the upper-left plot is shown. Note how the fraction of neutrons can drop to nearly 60% when hydrated with 25% water by volume. (lower-left) A histogram of the emission angle as a function of soil water content is shown. Note how the angular spectrum changes very little from that of a cosine distribution. (lower-right) A histogram of the emission radius as a function of soil water content is shown. Note how small the average motion in the soil is.

3. EXPERIMENTAL APPARATUS

As noted above, the apparatus is a two-element, liquid scintillator detector. An incoming neutron collides with a hydrogen nucleus (or carbon), and that recoiling proton (or carbon) deposits its energy within the scintillator. Similarly, a gamma ray photon can Compton scatter with an electron, and that electron deposits its energy in the scintillator. The remaining discussion assumes only elastic neutron collisions on protons and neglects carbon recoils and gamma interactions. The ignorance of carbon scatters is justified because carbon recoils only produce a fraction of the light a neutron-hydrogen scatter does due to strong quenching in the liquid scintillator chosen. This is despite the cross section for neutron-carbon scattering being comparable to that for neutron-hydrogen scattering (and liquid scintillator has roughly the same number of each species). The n-H and n-C scattering cross section for fast neutron energies is given in figure 10.

The cross section for scattering largely determines the bulk geometric design of the detector. The concept of a scattering length λ is more amenable to design considerations, and it can be derived from the cross section σ_i and number density n_i as

$$\lambda = \left(\sum_i n_i \sigma_i \right)^{-1} .$$

Note, that the total scattering length must be derived from the number density and cross section for each species *i*. By assuming a 4 MeV neutron enters a cell of liquid scintillator with water-like density and nearly equal number density for carbon and hydrogen (~5 × 10^{22} cm^{-3} in this example), then the total cross section is approximately 2 barns for n-H and n-C scattering. The total scattering length in this case is 5 cm. Therefore, a neutron traveling a distance x much smaller than this will have an interaction probability that is exponential $\exp(-x/\lambda)$, but a neutron traveling a distance much greater than this will likely scatter multiple times. It will be shown below that multiple scattering within a single cell degrades the ability to reconstruct a neutron event.

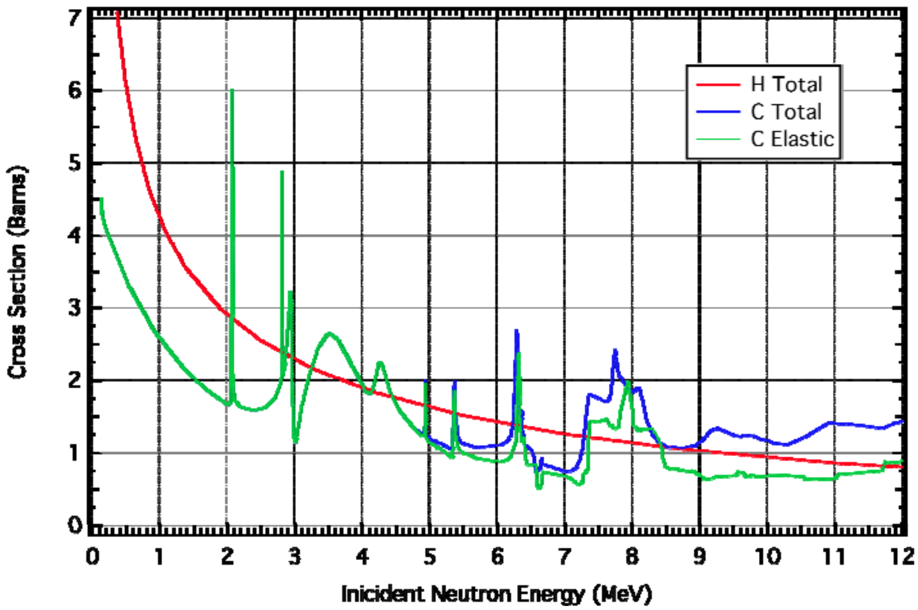

Figure 10: A plot that shows the total neutron cross section for interaction with hydrogen and carbon nuclei as a function of incident energy. The hydrogen cross section is entirely elastic in this energy range, but above approximately 5 MeV, carbon inelastic processes turn on.

Because the neutron and proton are essentially the same mass, elastic collisions are like billiard ball collisions. The energy deposit is uniformly distributed from 0 to its maximum energy. Very generally, if a neutron of mass m and energy E_{in} collides on a target nucleus of mass M (nearly stationary with respect to the neutron), the maximum energy transferred to the target nucleus $E_{\max}$ is

$$E_{\max} = \frac{4mM}{(m+M)^2}.$$

After interaction in a liquid scintillator, the neutron continues at a scattered angle with reduced energy where it can interact again.

Figure 11 shows a sample coincidence event from the ground plane. From the light output of the bottom cell, the proton recoil energy E_p can be calculated. After the first interaction, the neutron continues and interacts in the top cell. From the time-of-flight (TOF) between the first and second interaction, the energy of the neutron after the first scatter E_{out} is given by

$$E_{\text{out}} = \frac{1}{2} m_n v^2,$$

where m_n is the mass of the neutron, and v is the scattered neutron velocity. Due to the large size of the detector elements, the position information for the interaction is inexact. In this case, the distance traveled is assumed to be between the centers of the cells. Simulation can be used to estimate the uncertainty incurred by this assumption for a variety of geometries. Then, the incident energy can be reconstructed by the conservation of energy as

$$E_{\text{in}} = E_p + E_{\text{out}}.$$

Furthermore, the scattering angle follows from elastic scattering kinematics, and it is (all equivalent)

$$\sin^2\theta = \frac{E_p}{E_{\text{in}}},\ \cos^2\theta = \frac{E_{\text{out}}}{E_{\text{in}}},\ \text{and}\ \tan^2\theta = \frac{E_p}{E_{\text{out}}}.$$

It should be clear from this derivation that any deviation from the assumptions of single n-H scatterings in each cell would dilute the capability to perform spectroscopy or imaging.

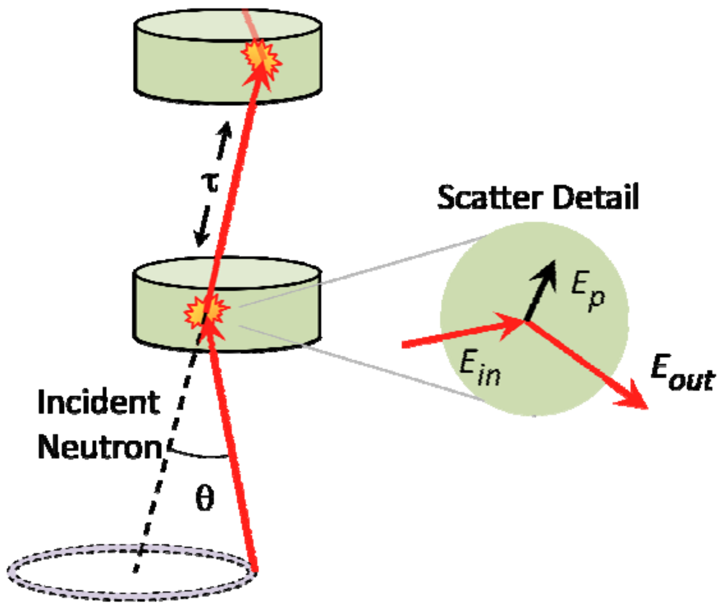

Figure 11: This diagram shows how a neutron detection event can be reconstructed. The details of the event reconstruction are given below.

The Mark I detector concept was two 2-inch diameter cylindrical cells 2 inches thick placed 6 inches apart with respect to cell centers. It is shown in the left picture of figure 12. The Mark I detector was found to have too low rate, and it was upgraded to Mark II. The cells in the Mark II detector are still 2 inches thick, but the diameter was increased to 8 inches. The distance between centers was also held to 6 inches. The Mark II detector is pictured in the right picture of figure 12. The entire liquid scintillator cell was made light tight and mechanically coupled to the magnetic shield of a 5-inch diameter, Hamamatsu H6527 photomultiplier tube (PMT) assembly. For completeness, the Mark I detector was of similar construction but used the 2 inch Hamamatsu H1949-51 PMT assembly. This manner of mounting improves ruggedization for field deployment. The DAQ, described below, was mounted on a standard, laboratory electronics rack.

Figure 12: The Mark 1 detector is shown in the left picture. It suffered from low rate, and it was upgraded to Mark 2 on the right picture. Note the improved overflow piston tube visible on the top detector. These were the first detectors of this design build by Sandia.

3.1. Liquid Scintillator and DAQ

Eljen EJ-309 liquid scintillator was chosen due to its favorable pulse-shape discrimination (PSD) between fast neutron interactions and gamma ray interactions. More information can be found at the vendor's website [25]. Each Mark 2 detector cell was completely filled with liquid scintillator. These detectors were the first of a new Sandia design that utilized a piston in an overflow tube to maintain the cell with 100% liquid. The previous Mark 1 design used an argon purge gas in the main cell to counter thermal expansion from environmental temperature changes. In the vertical orientation, this gas layer could degrade the optical coupling from the scintillator to the PMT glass, and this required a significant increase in PMT high voltage to compensate for the loss of gain.

The energy deposit per unit path length dE/dx for protons is a few orders of magnitude larger than for electrons, and the higher density space charge in the liquid scintillator promotes more rapid ionic recombination, thereby altering both the total light output in the scintillator (quenching) and the time structure of the light output pulse (PSD). Figure 13 shows the ranges for electrons and protons in vinyltolulene based plastic scintillator from the NIST ESTAR and PSTAR databases [26]. Plastic scintillator is a reasonable substitute to demonstrate the order of magnitude difference in ranges.

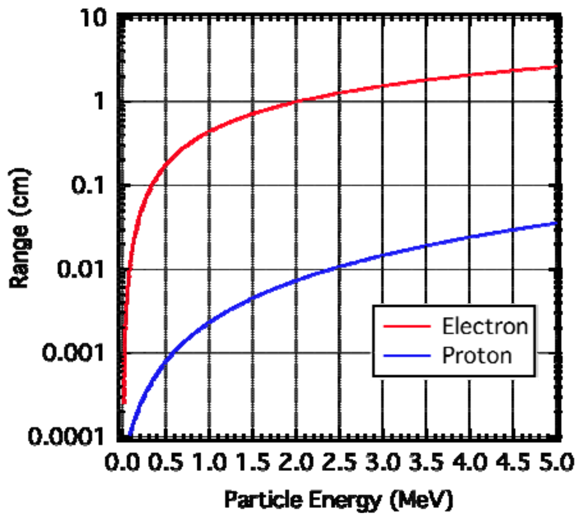

Figure 13: The range of electrons and protons in plastic scintillator as a function of energy is shown. The electrons range is nearly 100 times that of the proton.

Regarding the quenching, the electron energy deposit to scintillator light output is linear, but the proton energy deposit gives a non-linear response. For this work, a preliminary assessment from Enqvist *et al*. [27] was used to relate the proton energy deposit E_p to the equivalent electron energy E_e that produces the same light output L. A quadratic dependence is generally a good ansatz, and for EJ-309 it is

$$E_e = aE_p^2 + bE_p + c$$

where

$$a = 0.03495,\ b = 0.1424,\ c = -0.0362$$

This conversion formula from proton energy to electron equivalent energy is still uncertain, and there is ongoing work to measure it. Ignorance of its exact form does alter the reconstructed neutron energy spectrum as well as the scattering angle in this measurement. Also, variations in the light output could cause shifts even in simulation data. The use of a quadratic ansatz is fortuitous because it can easily be inverted.

Regarding PSD, the Mesytec MPD-4 NIM module was used to generate a both an amplitude signal and a PSD parameter signal [28]. It generates an amplitude signal by integrating the scintillation pulse, and it generates a PSD parameter by comparing the fast rise-time component of the pulse to the falling tail component. The MPD-4 is USB controllable so it can be optimized on the fly to a variety of different scintillators and geometries.

The implementation of the MPD-4 greatly simplifies the DAQ. A gate from each input channel is fed to a logic unit and a time-to-amplitude (TAC) module. The logic unit is set to coincidence events (requires a hit on detector 1 AND 2) or singles (requires a hit on detector 1 OR 2). This logic pulse then gates a peak-sensing ADC which records both amplitudes, both PSD parameters, and the TAC signal. Because we wish to record both events occurring from detector 1→2 or 2→1, the second signal is delayed such that an event occurring at the same time in detectors 1 and 2 will be occur in the center of the TAC full range. Figure 14 shows a block diagram of the data acquisition system. Finally, the DAQ is a computer controlled VME system run with National Instruments Labview.

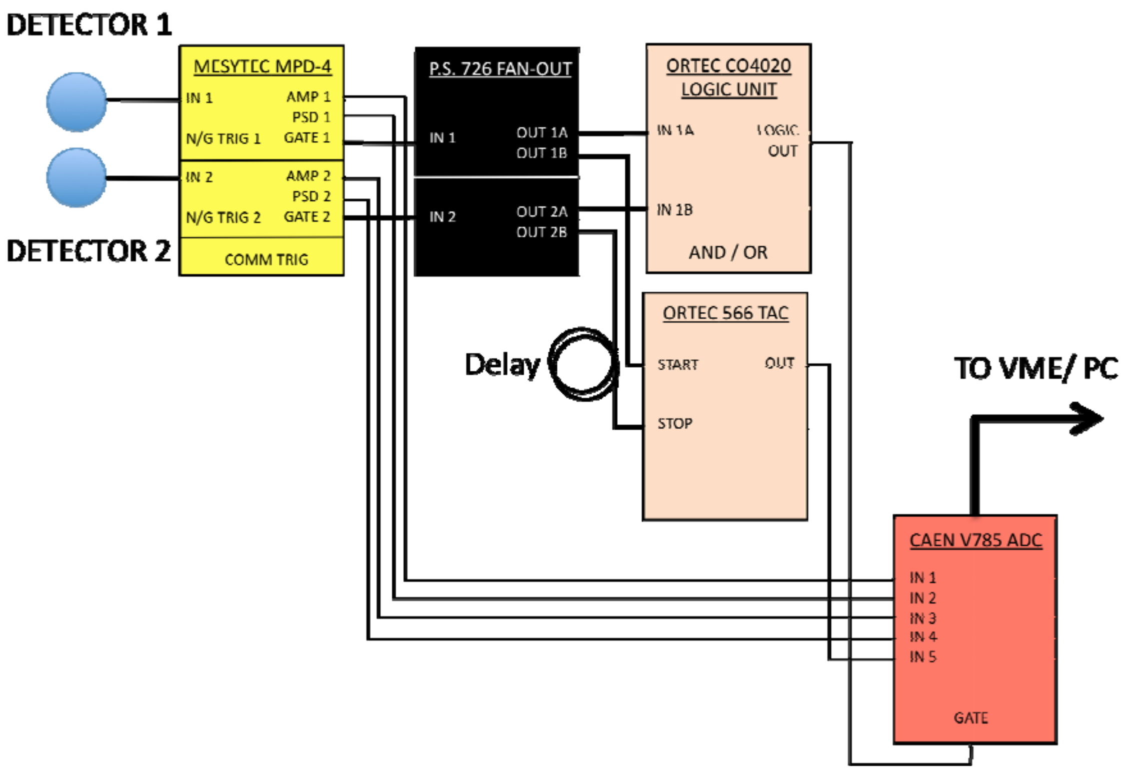

Figure 14: A block diagram of the DAQ is shown.

3.2. Calibrations

The calibration of the detector is a crucial step for optimized performance. An energy calibration with a gamma ray source (e.g. ^{22}Na, ^{60}Co, or ^{137}Cs) was used to calibrate the light output spectrum to the measured ADC channel spectrum. MCNP5 Monte Carlo simulation was required to calculate the expected electron energy deposit spectrum from the radioisotope source. This expected spectrum was fit to the ADC spectrum and the light output conversion was unfolded from the fit parameters.

The fit was a 9-parameter fit, and the Minuit fitting package within ROOT data analysis toolkit was used. First, the Monte Carlo spectrum shape was modified by 3 parameters: a gain, an offset, and an overall scale factor. Next, a Gaussian resolution was applied continuously at all energies E. The fractional width $\Delta L/L$ of the Gaussian resolution varied by a 3-parameter fit. It is

$$\Delta L/L = \sqrt{\alpha^2 + \beta^2/E + \gamma^2/E^2}$$

where α, β, and γ are the fit parameters. The first fit parameter arises from the transmission of light to the PMT, the second is the Poisson statistics of scintillation light production, and the last is from PMT dark current and amplifier noise. The physical significance of the resolution fit parameters is described in more detail in Dietz and Klein [29]. Finally, a 3-parameter power law background of the form

$$C(x + x_0)^n$$

is added to the fit. Figure 15 shows a sample energy calibration for ^{22}Na. The blue line is the raw Monte Carlo simulation, the magenta line is the power law background, and the red line is final response fit to the black data points. From these fits, the detector threshold is found to be approximately 100 keV, and this is set primarily by the MPD-4 hardware threshold.

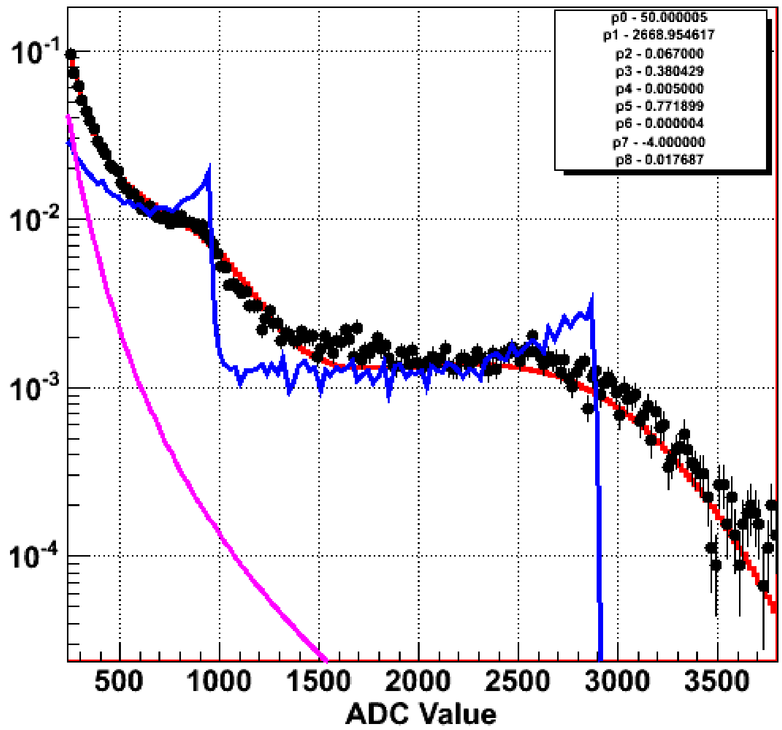

Figure 15: Sample ^{22}Na energy calibration fit is shown.

The pulse shape discrimination can also be calibrated with a mixed neutron and gamma source (e.g. ^{252}Cf, AmBe, or background). For a given ADC channel bin, neutron-like events will have PSD parameter values that tend to accumulate in a Gaussian region separated from another Gaussian region of gamma-like events. The center and width of these Gaussians is found as a function of ADC channel. A sample fit is shown in figure 16.

During experimental running, a given event will have both an ADC channel E and a PSD parameter value N. Suppose the center and width of the neutron and gamma Gaussians are given by $\overline{N}_n(E)$, $\sigma_n(E)$, and $\overline{N}_g(E)$, $\sigma_g(E)$, respectively. Then a relative probability of it being a neutron or gamma is given by

$$P_i = \exp\left(\frac{-\left(\overline{N}_i(E) - N\right)^2}{2\sigma_i^2}\right)$$

for i=neutron or gamma. The likelihood L_n of being a neutron is then $P_n / \sum P_i$; the likelihood L_g of being a gamma is then $P_g / \sum P_i$. Other likelihoods can be added into the sum, e.g. the likelihood for a minimally ionizing muon is a typical candidate.

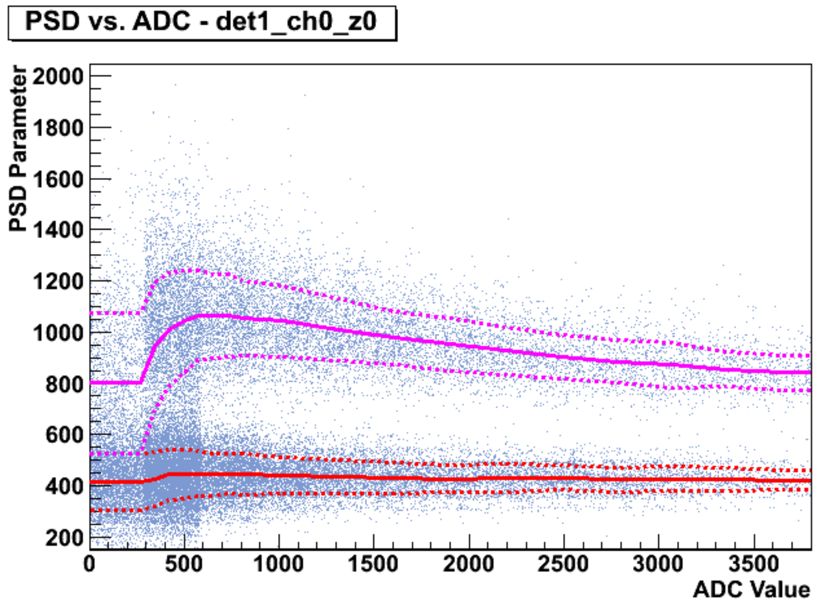

Figure 16: AmBe calibration of the detector PSD is shown. The upper band is the 1-σ Gaussian width of the neutron-like events. Similarly, the lower band is the gamma-like events.

Finally, there can be relative time delays between the pair of detectors. By placing a gamma source behind each detector, coincidences from 1→2 and 2→1 will yield two peaks in timing. The average of these peak locations gives the necessary trim required to cancel out this relative timing delay. Figure 17 shows a sample timing fit.

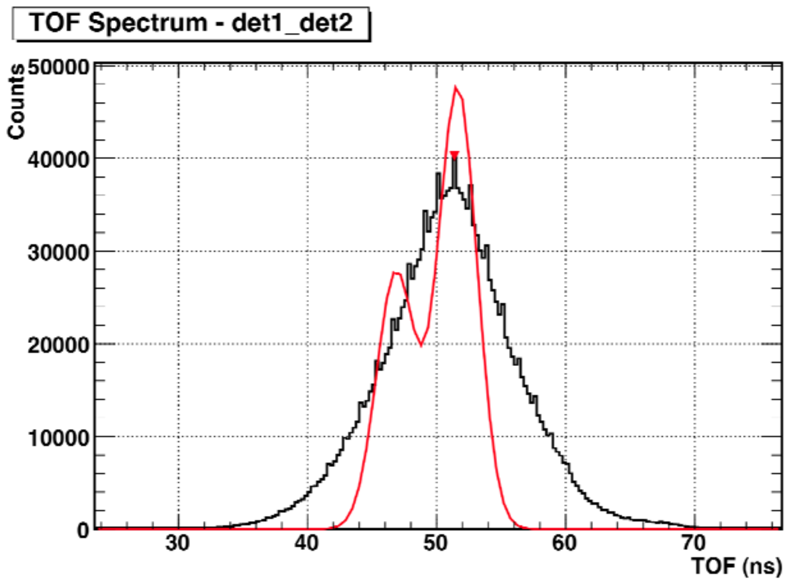

Figure 17: The TOF calibration is shown.

4. RESULTS

Before attempting to measure any background neutrons in the environment (or the laboratory), the performance of the system was benchmarked with radioisotope sources. An AmBe source was used as a neutron source in all tests described below as a matter of convenience. The calibration procedures are described above, and they were performed; these AmBe source tests move beyond those calibrations.

4.1. Preliminary Measurements

An initial scoping measurement was performed with the AmBe source place near one of the cells and away from the other. Initially, simple cuts were made to eliminate any events that caused the ADC, PSD, or TAC to have saturated values or pedestal values. For single events in the liquid scintillator, the likelihood derived from the PSD can be used to cut out gamma-like events. Figure 18 (left) shows the number of events from the AmBe source versus its likelihood. The peak of neutrons near 100% likelihood indicates a good discrimination of events in this detector. A coincidence of events can also be assigned a neutron likelihood, and it is shown in figure 18 (right).

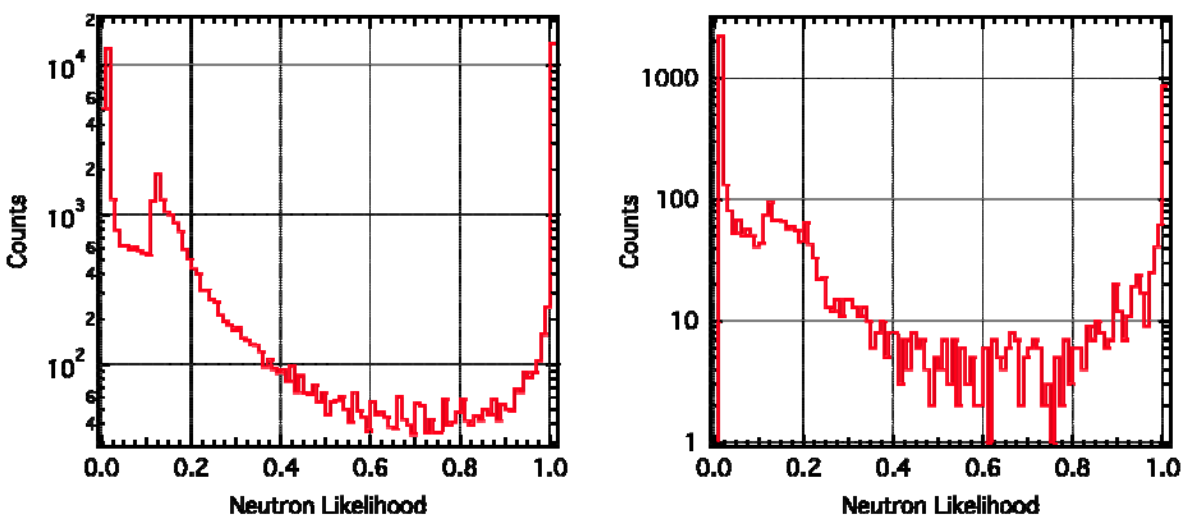

Figure 18: Histograms of the neutron likelihood for a single detector hit (left) and for a coincidence of hits (right) for an AmBe source are shown.

By cutting on events below likelihood 97.5%, the gamma contamination is greatly reduced. Figure 19 shows the PSD parameter versus the electron equivalent energy (MeVee) before cuts (left) and after cuts (right) for a single detector. Because coincidence events are of particular interest in imaging, it is useful to see how the neutron likelihood cut affects that analysis. Figure 20 shows histogram of the PSD parameter of the first detector versus the PSD parameter of the second detector before the neutron likelihood cut (left) and after cuts (right).

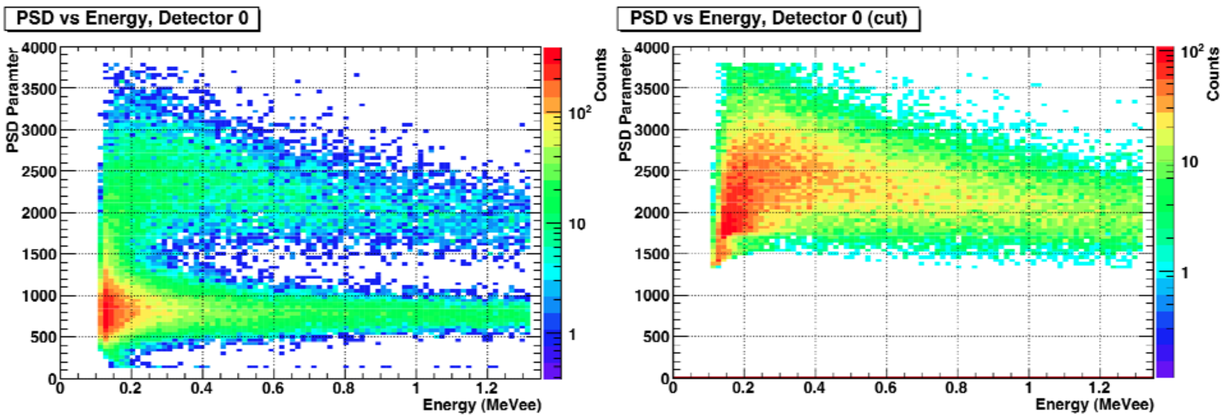

Figure 19: (left) Histogram of PSD parameters versus electron equivalent energy (MeVee) before a neutron likelihood cut of 97.5% and (right) after cuts are shown.

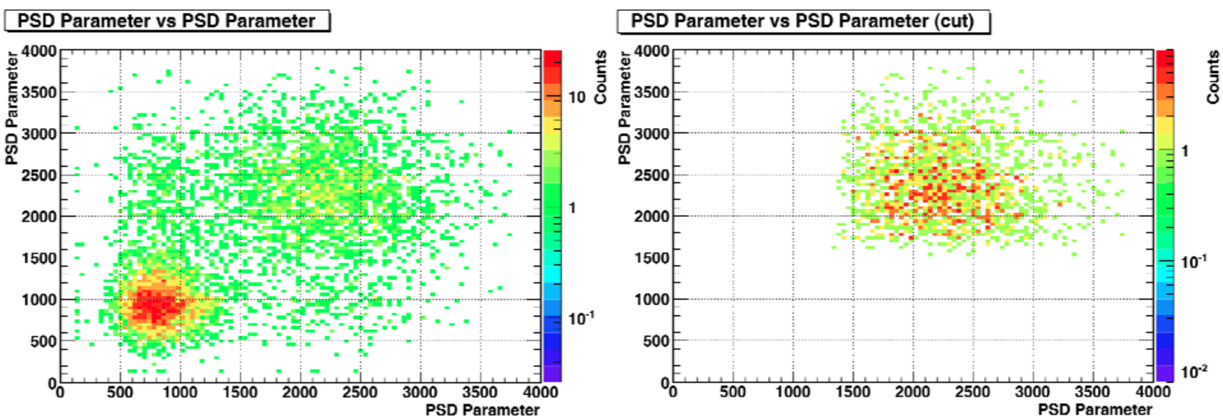

Figure 20: (left) A histogram of the PSD parameter of the first detector versus the PSD parameter of the second before the neutron likelihood cut and after the cut (right) is shown.

For coincident events, the likelihood can be used to reject gamma events, but the TOF should be vastly different for a few MeV neutron and gamma ray. Figure 21 shows the TOF spectrum before and after the neutron likelihood cut. The application of the likelihood cut is very effective at rejecting events with TOF too fast to be real neutrons. In fact, the longer TOF events that should be coincident neutrons are relatively unaffected, which is indicative of a good cut. The preponderance of negative TOF events implies that the source is located on one side of the detector assembly, and this was the case.

The application of the likelihood cut would seem to suggest that the TOF alone could be effective at rejecting gamma events. The use of an AmBe source belies the potential difficulties with this approach. First, there are an overwhelming number of neutrons from the AmBe source such that neutron signal relative to the gamma signal is much larger than the natural background. The neutron signal thus overwhelms the accidental coincidences from two uncorrelated events (neutron-neutron, gamma-gamma, or gamma-neutron). If accidental collisions are a significant source of coincidences, then event-by-event analysis becomes more difficult. Accidentals are expected to be uniform across the entire TOF spectrum, so there may be recourse to an aggregate analysis where the accidental spectrum is subtracted. More on this will be discussed in the Conclusions of this report.

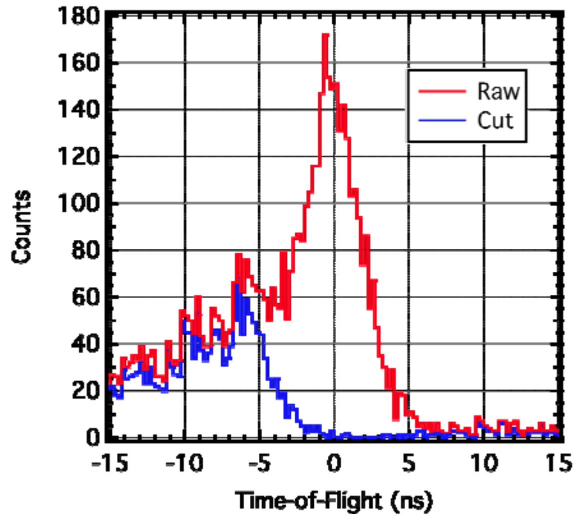

Figure 21: A histogram of the TOF between coincident events is shown before and after the neutron likelihood cut is made. The likelihood cut successfully removes events that have timing too fast to be a real neutron.

4.2. Angular Response

Another series of tests were made to measure the response of the detector to the AmBe neutron source as a function of angle (with respect to the center of the apparatus). The detector was rotated horizontally, and it and the AmBe source were elevated off the floor to reduce the effect of floor scatters. The AmBe source was located 24 inches from the center of the detector and placed at angles of 0°, 30°, 45°, 90°, 120°, and 180°. A diagram of the setup is shown on the left of figure 22.

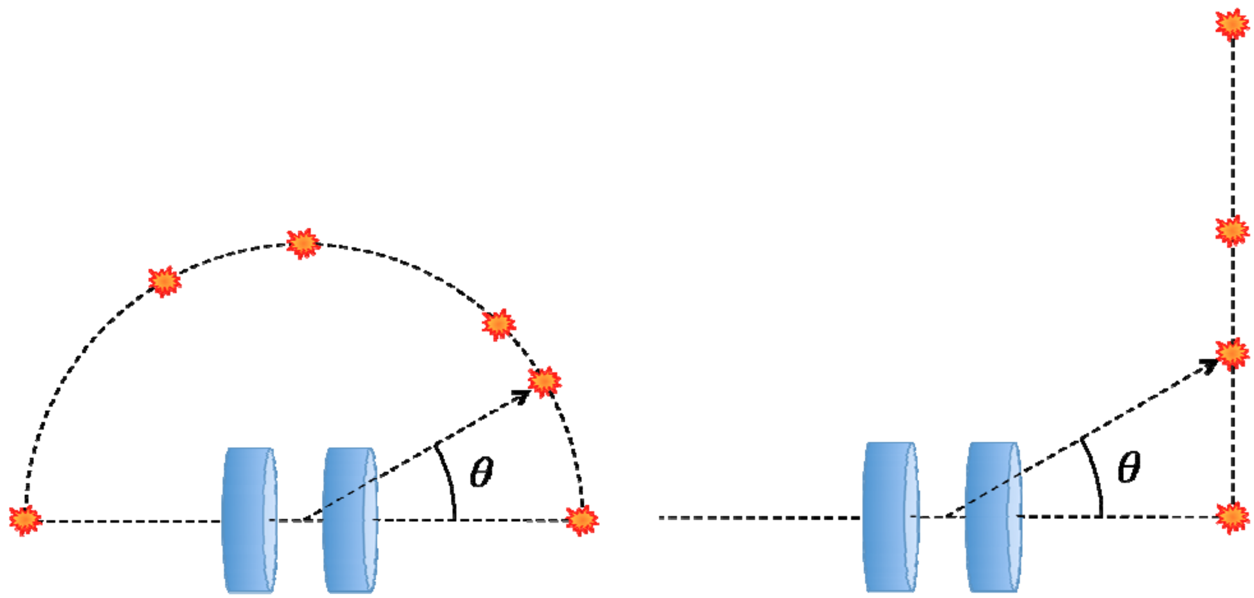

Figure 22: (left) A schematic diagram is shown of the source locations used to measure the source angle response of the detector. (right) A schematic diagram is shown of the source locations used to measure the plane angle response of the detector.

The scattering angle can be calculated on an event-by-event basis by assuming single elastic scatters on hydrogen. The results from the AmBe data are shown in figure 23. The figure on the left is the rate from the data, and on the right, each histogram is normalized to illustrate the shape change as the source angle changes. The scattering angle distribution does seem to change with source angle, though weakly. This is expected due to the large size of the detectors.

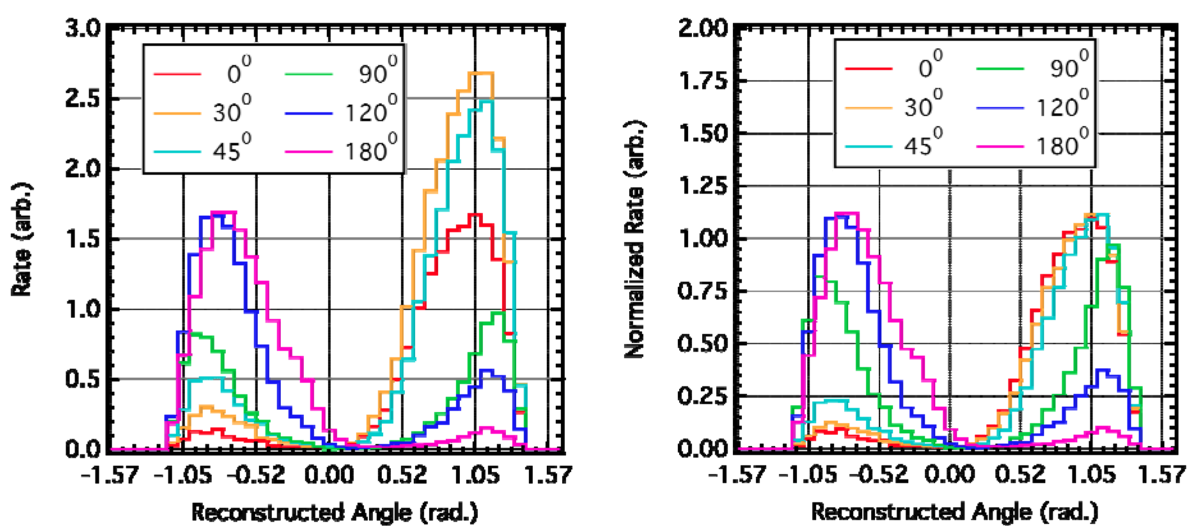

Figure 23: (left) Histograms of the angular response rate data are shown. (right) The same histograms have been normalized to illustrate the shape change in the reconstructed angle.

Because the detectors are large and relatively close together, there is a large spread of possible scattering angles that can be detected. A simple simulation was done to determine the possible range. In this simulation, a random point was selected uniformly in each detector, and the required scattering angle was calculated given the incoming source direction. This scattering angle was then weighted by the probability for elastic scattering into that angle. This calculation is very simple because it does not include carbon collisions, multiple scattering, etc. It is apparent that even in this idealized calculation, the reconstructed scattering angle is only marginally separated. A full Monte Carlo was also performed, and with these complications, the separation of the scattering angle is diluted. These results for a neutron traveling at 0° and 90° angle of incidence are shown in figure 24.

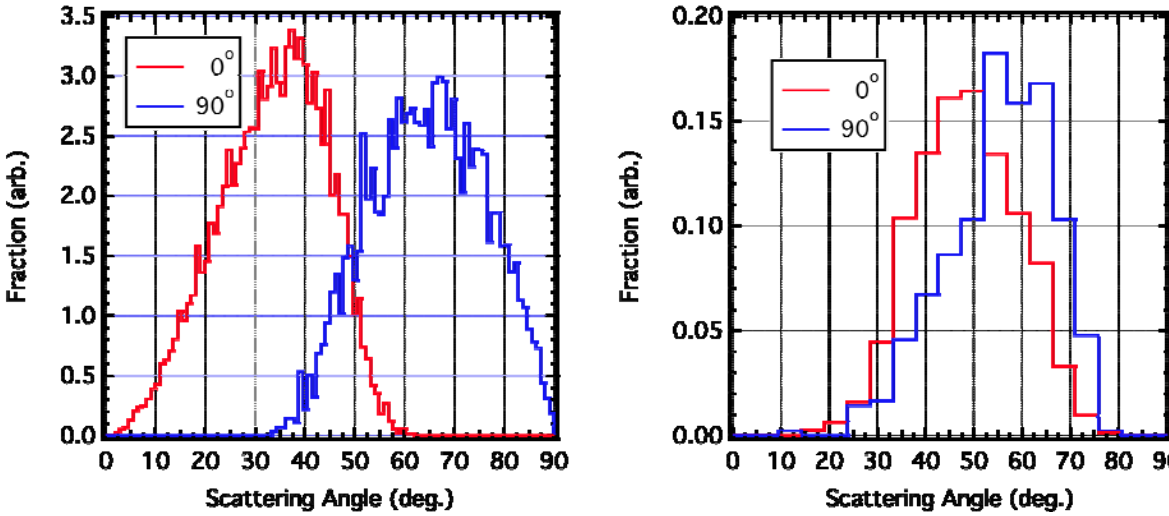

Figure 24: The distribution of scattering angles is shown for a 0° and 90° incident neutron (red and blue, respectively) are shown for a simple calculation (left) and a more detailed Monte Carlo simulation (right).

The cutoff at approximately 1.2 radians (~70°) is due to the TOF cutoff at 16 ns that is due to an error in the initial TAC and ADC settings. Future experimental runs will expand the timing window, and that should remove the scattering angle cutoff.

Monte Carlo simulations were also undertaken to understand the angular response of the detector. MCNP5 was used, and the ISO-8529-1 standard neutron spectrum was used as the input for the neutron energy spectrum [30]. Figure 25 shows Monte Carlo comparisons to data for the 0°, 45°, 90°, and 120°. The Monte Carlo results agree with data qualitatively, though there are some discrepancies that require explanation.

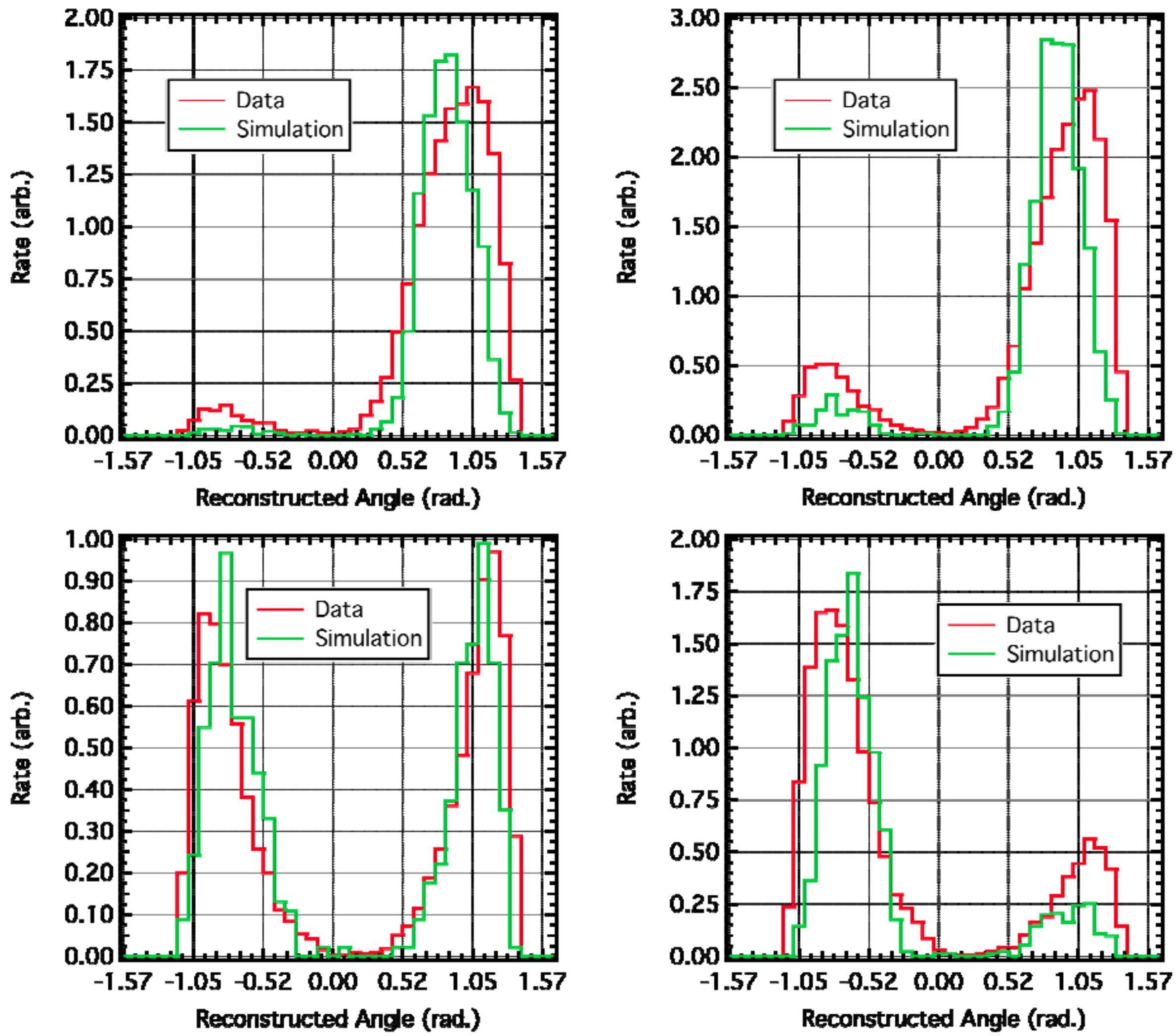

Figure 25: Histograms of the reconstructed scattering angle data versus Monte Carlo simulation for 0° (upper-left), 45° (upper-right), 90° (lower-left), and 120° (lower-right) are shown.

An interesting consequence of a two-element detector is that the number of forward (> 0°) and backward (< 0°) events can be used to "image" the AmBe source. It is clear that as the source rotates around the apparatus, the scattering angle modulates in a measurable way. The current agreement between the data and simulation notwithstanding, the detector is a promising neutron imager.

Motivated by the aggregate event counting discussed above, singles and coincident count rates can supplement event-by-event imaging. The coincidence rate as a function of source angle is shown in the left plot of figure 26 and the singles rate is shown on the right. The MCNP5 simulation is appended as well as a naïve solid-angle calculation. The solid-angle result does not include shadowing of one cell in front of another, interaction probability due to depth, nor the PMTs. Its failure does suggest why the MCNP5 Monte Carlo simulation (which includes shadowing, multiple scatters, etc.) also fails at small angles. The MCNP5 simulation does not include the PMTs, nor the surrounding aluminum detector stand, and the data seems to suggest the PMT attenuates the source at small source angles relative to larger source angles. Future simulations must incorporate more components of the detector structure.

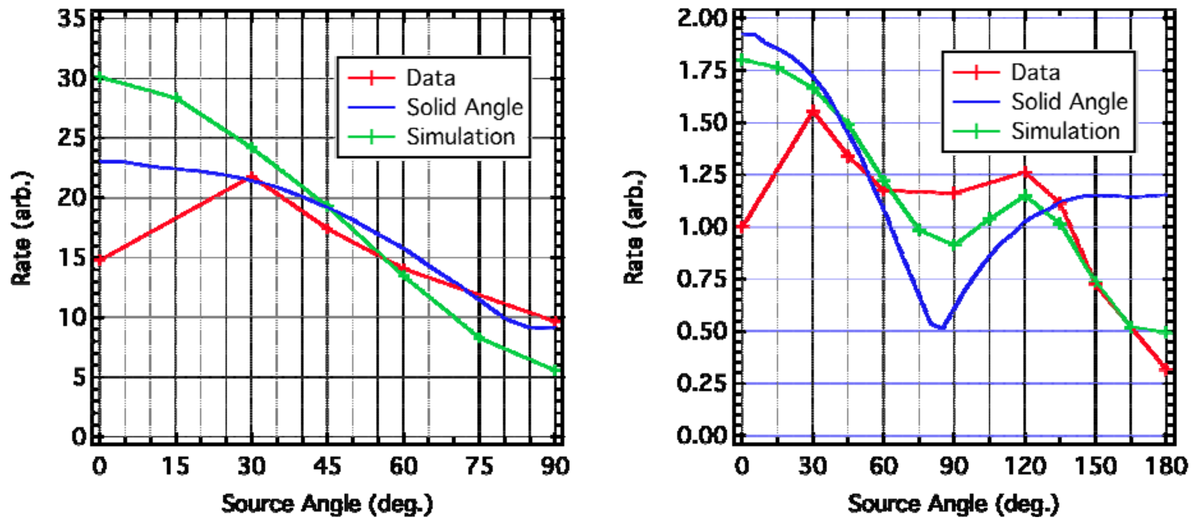

Figure 26: (left) The coincidence rate as a function source angle is shown. By assuming a symmetric detector the 0° to 180° range can be reduced to 0° to 90° range. The 120° data then substitutes for 60° data and the 0° and 180° data have been averaged. (right) The singles data rate for the near detector (nearest to the source at 0°) is shown. The plot assumes symmetry for the far detector, and its response is at θ is the same as the near detector at 180°- θ. Each plot contains the naïve solid angle estimate as well as the full MCNP5 Monte Carlo simulation.

4.3. Planar Response

Because the detector is intended as a soil water "imager", the response to a rotated source is somewhat contrived. The response to a planar source is a more appropriate figure of merit. Referring back to figure 22, the planar response to an AmBe source was measured at angles of 0°, 30°, 45°, and 60° on a plane 24 inches away from the detector center.

Similar to the previous section, the scattering angle reconstruction rates from the data are shown in figure 27. The plot on the left is the relative rates for each source angle, and the plot on the right is the normalized rate to illustrate the shape change. Again, the shape does change somewhat as the angle is increase, and this suggests a way to image a source on an event-by-event basis. The scattering angle reconstruction from the data is compared to Monte Carlo simulation in figure 28. Again, the agreement is qualitatively good, though, better agreement is expected when the PMT is effectively modeled in the simulation.

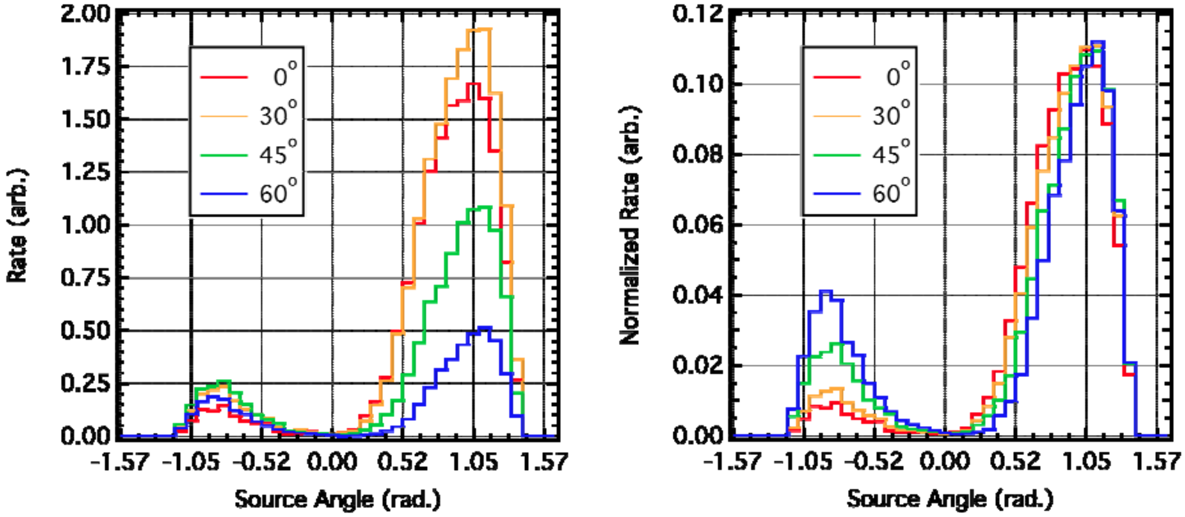

Figure 27: (left) Histograms of the planar response rate data are shown. (right) The same histograms have been normalized to illustrate the shape change in the reconstructed angle.

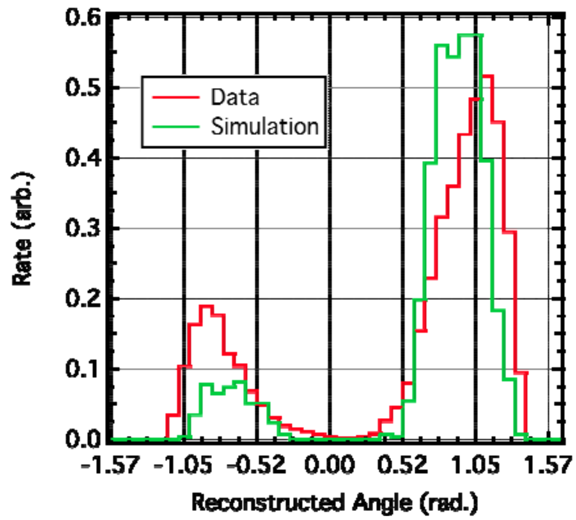

Figure 28: The agreement between Monte Carlo simulation and data is similar in the planar data to the previous angular rotation study. The 60° data is shown for comparison.

In the planar geometry tests, scaler-counting rates are an important handle on the detector data. Figure 29 shows the coincidence count rate as a function of planar angle. The figure also contains the solid angle calculation estimate and the MCPN5 simulation. Here, the naïve solid angle calculation, simulation, and data are in excellent agreement beyond 60°. The singles rates for the near and far detector are shown in the left and right plots of figure 30, respectively. Again, agreement is good at larger angles with the model and simulation.

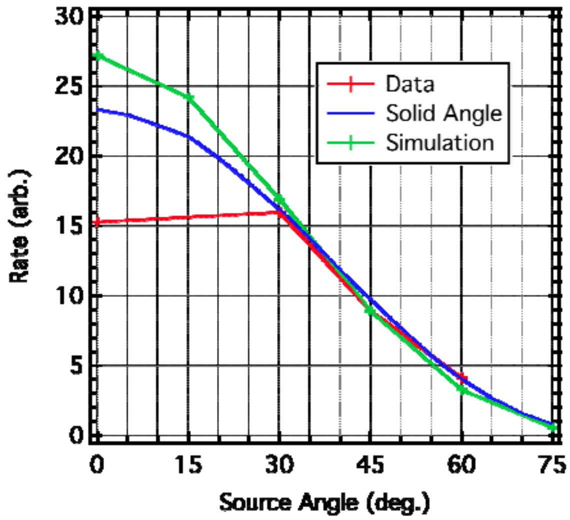

Figure 29: The coincidence rate as a function of planar angle is shown. Similar to figure 26, the agreement between all models to the data is better at larger angles where shadowing and neglect of the PMTs has a smaller contribution.

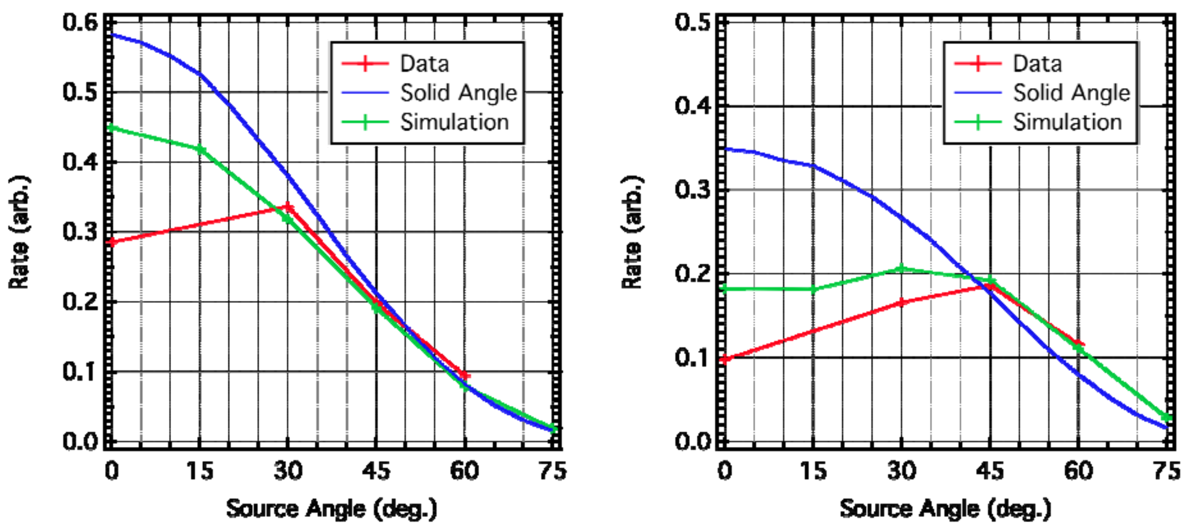

Figure 30: The singles rate as a function of planar angle is shown for the near detector (left) and the far detector (right). The poor agreement at small angles is evidence of cell-to-cell shadowing and the neglect of the PMTs in the model.

These tests are measurements of the point source detection efficiency $\varepsilon(\rho)$ as a function of radial distance on the ground from the detector axis ρ. Assuming that a swath of soil has uniform source strength of neutrons, then the point source detection efficiency must be scaled by $2\pi\rho$ because concentric rings of soil will emit more neutrons, as the radius ρ gets larger. To derive the expected count rate for small ρ (small planar source angle), $\varepsilon(\rho)$ must be linearly fit because the simulation is inadequate at small angles. At larger angles, the solid angle approximation is an adequate as a model for $\varepsilon(\rho)$, and it is given by

$$\varepsilon(\rho) \sim \frac{1}{\rho^2 + (h \, \mathrm{m} d/2)^2} .$$

Here, h is the distance of the detector center to the ground plane (24 inches in this test), d is the distance between cell centers (6 inches in this test), and the negative (positive) solution is for the near (far) detector from the plane. Therefore, at large distances, the singles counter results from the first section is recovered.

Figure 31 shows the results of the radially-corrected count rate. Despite a crude interpolation for the small-angle data, it is clear that the count rate response is maximal for radii approximately equal to the distance from the detector to the ground plane. This does not differ significantly from the single detector count rate. This result strongly motivates the event-by-event approach because a simple counter has a response that is

$$C(\rho) \sim \frac{\rho}{\rho^2 + h^2}.$$

Analyzing event-by-event can circumvent this problem by monitoring the count rate in specific radial bins $C(\rho_i)\Delta\rho_i$.

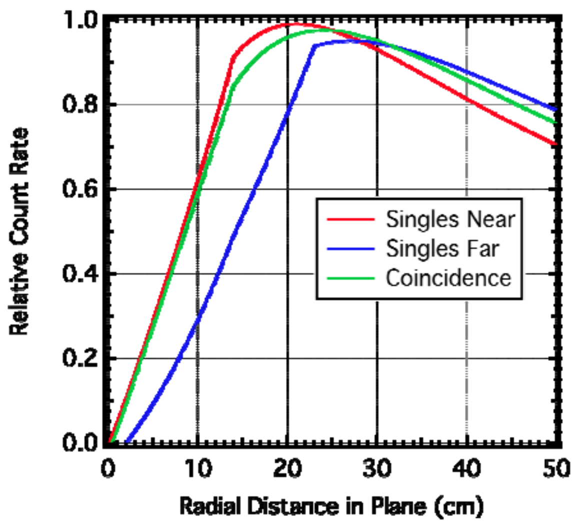

Figure 31: The relative radial response ($2\pi\rho$ corrected) of the near and far detector in singles and coincidence events is shown.

An additional result that could be utilized from figure 31 is the suppressed response of the far detector at small ρ. The shadowing of the far detector by the near detector reduces its detection efficiency at small ρ, which essentially increases the relative response at larger ρ. These naïve assumptions fail to accommodate the angular response of the soil. The outgoing angular scatter distribution from the soil is a cosine distribution (shown in figure 9), not a point source as assumed in this type of calculation. Furthermore, the response has assumed that neutrons are not attenuated from a distant source point as they travel towards the detector. The range is on the order of a few hundred meters in air, and this also modulates the detector response.

4.4. Energy Spectroscopy

An added benefit of coincidence measurements is the ability to reconstruct the energy spectrum of a source. Figure 32 shows the data versus theory for an AmBe source and background on the left and right plot, respectively. The comparison of these two data sets is shown together on figure 33. The detector is able to differentiate the two different energy spectra.

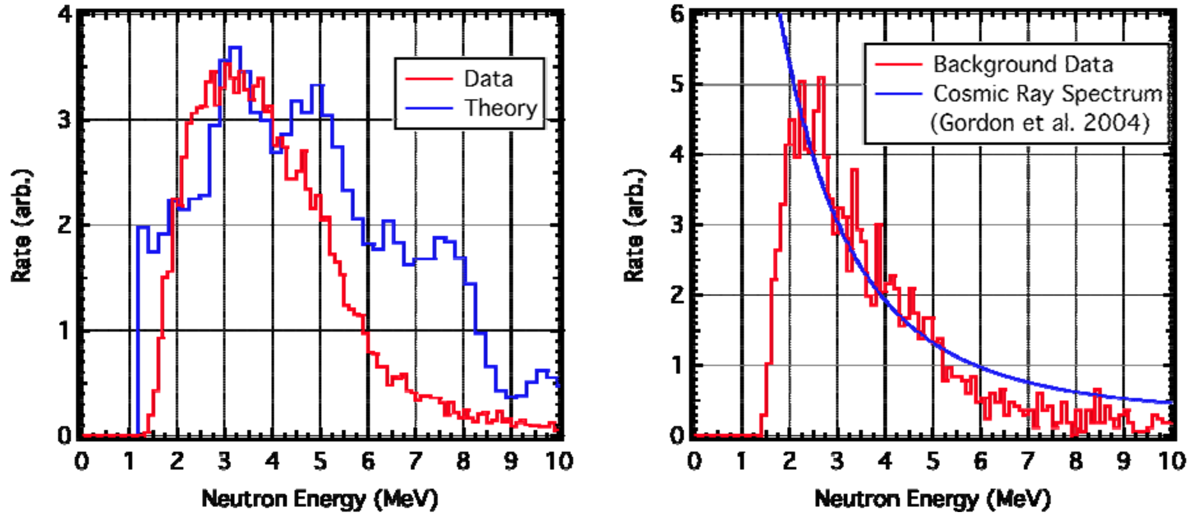

Figure 32: (left) Histogram of reconstructed neutron energy for an AmBe source versus theory is shown. (right) Histogram of reconstructed neutron energy for background versus the Gordon *et al*. parameterization of the background is shown.

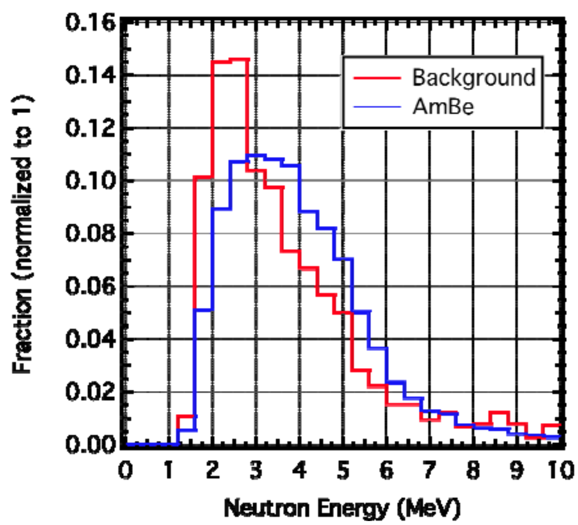

Figure 33: A comparison of the AmBe and background data is directly compared on this plot.

The disagreement of the reconstructed energy at higher energy, especially for AmBe, is not unanticipated. Another simple calculation can be performed that is similar to the one used to generate figure 24. In this case, given a specific TOF, the distribution of possible energies can be generated and compared to that generated from simple cell centers. The results are shown in figure 34. The average reconstructed energy is nearly 50% larger than the cell-to-cell estimate would expect. Therefore, it seems reasonable that the E_{out} contribution to E_{in} could be scaled to a larger value to reflect this average. A full simulation is underway to investigate this.

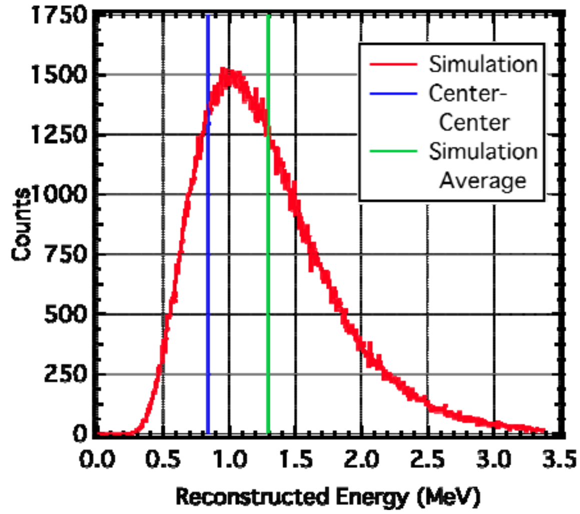

Figure 34: The spread of possible energies given a specific TOF is shown. The blue line is the energy estimated for events occurring between cell centers, and the green line is the average of the distribution.

4.5. Source Imaging

As a final test of the detector capabilities, the 0°, 30°, 90°, 120°, and 180° were used to generate an angular response map for every 30°. This entailed "flipping" the 120° to generate a 60° data set, and "flipping" the 30° for a 150° data set. Because the detector is not perfectly symmetry (gain differences, thresholds, etc.), this may result in a worse imaging capabilities. Then, the 45° data was fit to see how well this course response map would image the source. Figure 35 shows the result of this fit (left) the fit parameters (right). We see that the fit parameters are spread over the correct region with no contamination from the "wrong" direction.

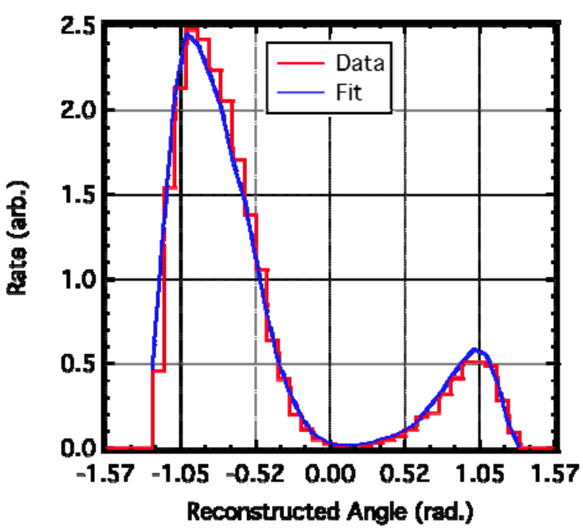

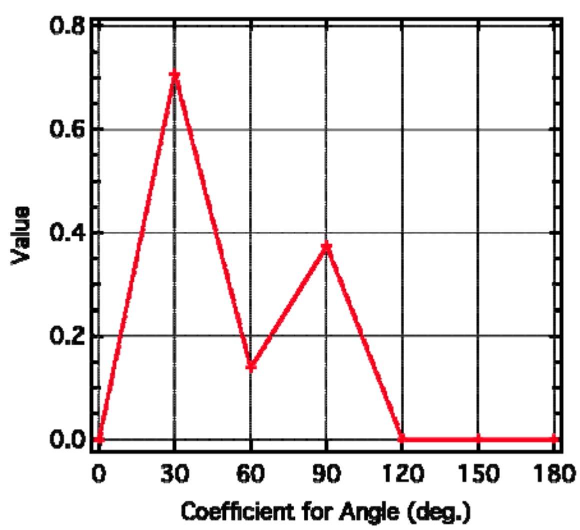

Figure 35: The reconstructed angular distribution for an AmBe source at 45° is shown on the left. The fit uses response functions for every 30°, and the fit contributions are shown on the right.

4.6. Laboratory Backgrounds

The detector was setup in the laboratory to collect background events. Approximately one week of coincidence-only data was obtained in late February with the detector in a horizontal configuration. Another week of singles data was obtained in early May with the detector in its vertical orientation. Unfortunately, direct comparison of these data sets is complicated by the fact that thresholds and gains were changed in order to further optimize the detector. It is noted that the data below have their reconstructed angle flipped with respect to the AmBe response files.

The horizontal detector data and its fit to the AmBe source response is shown in figure 36. The predominance of less than 90° components is consistent with the distant source locker of the laboratory contributing a residual number of above background counts. Because the detector is horizontal, it is expected that the 90° response is the largest as is seen.

Figure 37 shows the data, fit, and fit coefficients for the detector in its vertical orientation. Here, the fit is a bit muddled. It is reassuring that the response is relatively flat. Finally, figure 38 is the same as the background run, except the area of the floor under the detector was layered with 2 inches of a high density polyethylene (HDPE) to moderate fast neutrons in a similar manner to water. The results are very similar to the non-shielded data. There may not have been enough HDPE to affect the spectrum significantly.

Examination of the singles rates is also inconclusive because of spikes in the detection rate versus time. Because this was tested in an active laboratory with potential incidental source motion, this is anticipated. It is difficult to interpret possible variations in the data because of this, but it is encouraging that the detector has a high level of sensitivity.

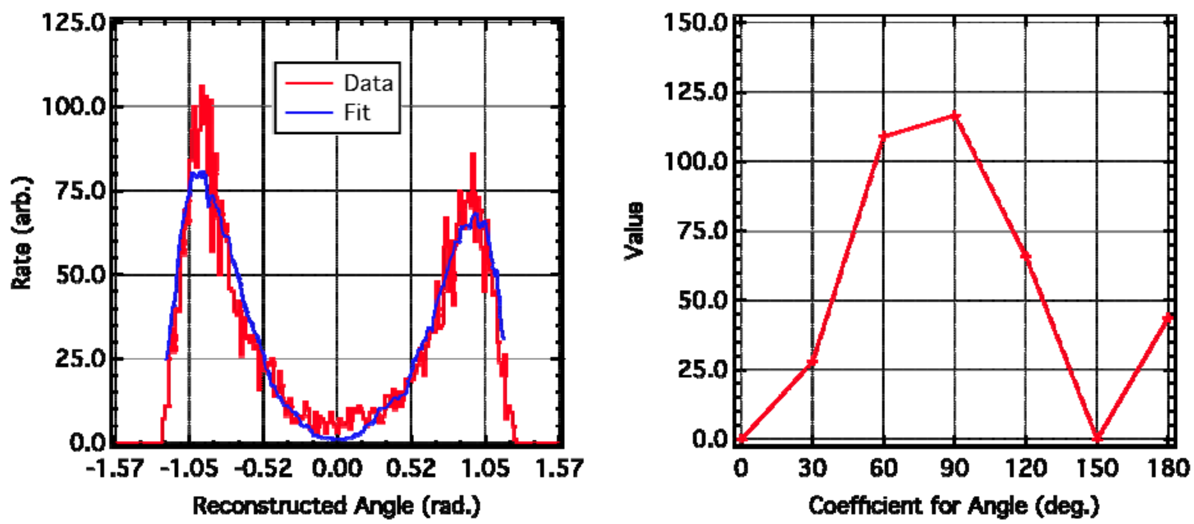

Figure 36: The reconstructed angular distribution for the laboratory background is shown on the left. The detector is in a horizontal orientation. The fit uses response functions for every 30°, and the fit contributions are shown on the right.

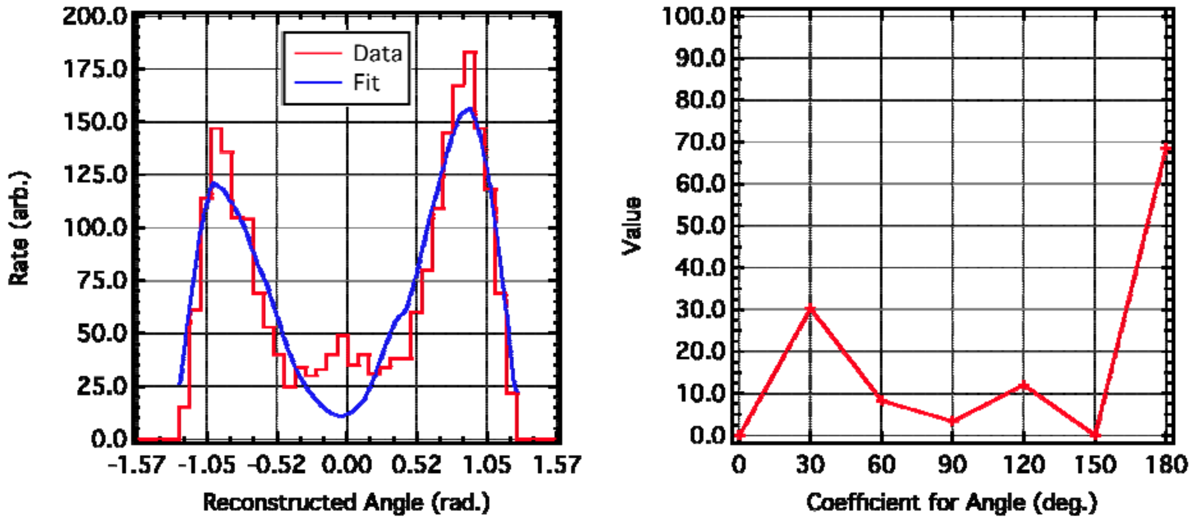

Figure 37: The reconstructed angular distribution for the laboratory background is shown on the left. The detector is in the nominal vertical orientation. The fit uses response functions for every 30°, and the fit contributions are shown on the right.

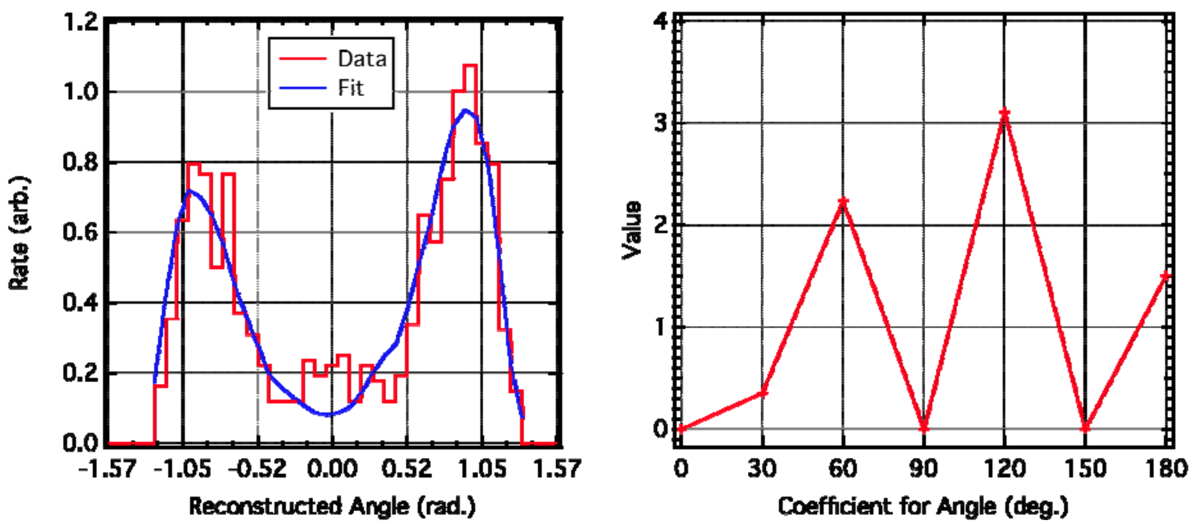

Figure 38: The reconstructed angular distribution for the laboratory background is shown on the left. The detector is in the nominal vertical orientation. The fit uses response functions for every 30°, and the fit contributions are shown on the right.

For completeness, the singles rates for the vertical orientation are very encouraging. Nearly 1000 neutron coincidences were recorded per day. Over 10^5 neutron singles were recorded during the day. It is hoped that the singles rates of the top and bottom detector could be used as a relative gain monitor, allowing the detector to be calibrated *in situ*. Furthermore, the directionality of the detector coincidences allows the ground scatter rate to be directly compared to the overhead cosmic ray background rate. This is a feature not possible a single detector.

Finally, the affect of water was considered in a controlled laboratory test. An AmBe source was placed on the ground 2 meters from the detector axis; the detector was 1 meter above the ground.

The AmBe source was shielded to block direct line-of-sight to the detector, thereby artificially forcing ground interactions. At that ground location, tests were recorded with nothing, 1.5 inches of water in a catch pan, and HDPE blocks. While the effect was slight, the recorded coincidence counts did drop with the addition of the small pail of water and more with the use of thick HDPE blocks. As expected, the angular distribution does not change significantly as the experiment is assembled.

5. CONCLUSIONS

This SAND report is being written approximately one year after the project's inception due to the primary investigator leaving Sandia. It was initially granted two years of funds. The success of the project must rely, in some sense, upon a projection of only half the work that would have been performed. This half of the work has some exciting conclusions to not only the expressed written purpose of measuring the cosmic ray neutron background, but to the general radiation detection goals of the 8132 group.

The detector concept has achieved nearly all the first year milestones. A working model of the soil response to the cosmic ray neutron spectrum has been completed. There is a strong modulation of the fast neutron spectrum when modest amounts of water are introduced. The detector is most sensitive to the region where the modulation is greatest (~1-5 MeV).

Using laboratory tests with radioisotopes, a two-element liquid scintillator detector was developed that could effectively reject gamma backgrounds and measure both singles and coincidences of neutron events. Using an AmBe neutron source, the imaging and energy spectroscopy capabilities of the detector have been identified. The detector can identify to at least 30° along the axis of symmetry in an event-by-event method. If the aggregate number of counts causing a coincidence in one direction is compared to the other, the fraction can precisely determine the direction of a single source. Figure 39 shows this for the data and Monte Carlo simulation.

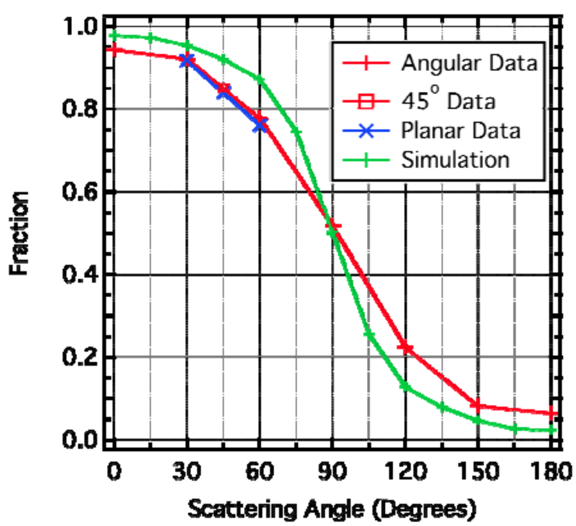

Figure 39: The fraction of coincidence events that are "forward" to the total is shown for the angular response data and Monte Carlo. Overlaid is the planar data that shows that it behaves similarly.

The most important result is the relatively high rate of neutrons available for analysis. This was one of the technical risks to this approach, and it is reasonable to assume that the fast neutron detector can be further optimized.

5.1. Future Work

Because the project is being terminated early, there are still many milestones to achieve. Well motivated in the body of this report is the need to improve the Monte Carlo simulation. Specifically, the presence of the PMT modulates both the singles spectra (strongly along the detector axis) and the coincidence spectrum.

In order to full utilize the coincidence spectrum that is unique to this approach, the imaging capabilities must be enhanced. Improving the Monte Carlo will improve our understanding of the detector, and as has been shown, measuring the AmBe angular response has been crucial. A new imaging technique that could be applied is the maximum likelihood estimation technique (MLEM) [31]. Figure 40 shows the detector response for use in an MLEM maximization algorithm. Preliminary tests are very encouraging.

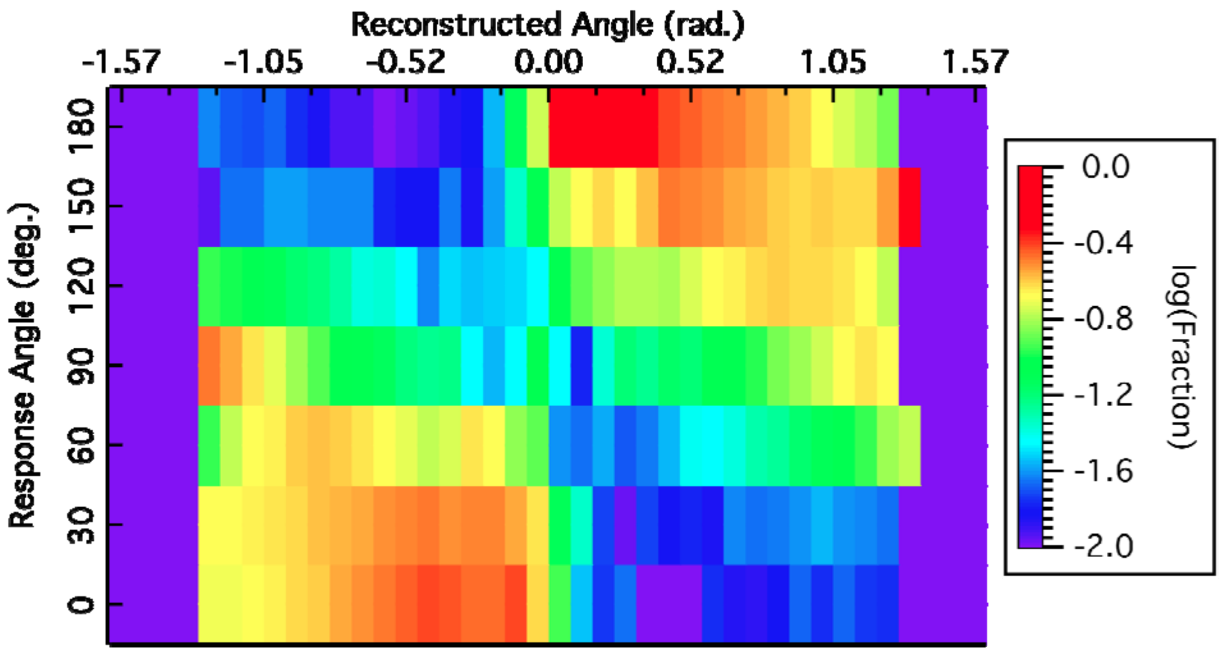

Figure 40: The relative likelihood that a given angular reconstructed event comes from a source at a given location is shown. This could be used an MLEM response map to "unfold" the true source spectrum.

Finally, there is work underway to test the effect of cell spacing on both the detection rate and the imaging / spectroscopic capabilities. It is expected that reducing the spacing will increase the rate at the expense of imaging capability. Optimizing the Monte Carlo will be an important supplement to this work.

6. REFERENCES

1. S.K. Tanaka, *et al*., *Climate Warming and Water Management Adaptation for California*, Climatic Change **7** (2006) pp. 361-387. doi:10.1007/s10584-006-9079-5

2. W.C. Feldman, *et al*., Global Distribution of Neutrons from Mars: Results from Mars Odyssey, Science, **297** (2002) pp. 75-78. doi:10.1126/science.1073541

3. I. Mitrofanov, *et al*., Maps of Subsurface Hydrogen from the High Energy Neutron Detector, Mars Odyssey, Science **297** (2002) pp. 78-81. doi:10.1126/science.1073616

4. W.V. Boynton, *et al*., *Distribution of Hydrogen in the Near-Surface of Mars: Evidence for Subsurface Ice Deposits*, Science **297** (2002) pp. 81-85. doi:10.1126/science.1073722

5. A.W. Western, R.B. Grayson, and G. Blöschl, *Scaling of Soil Moisture: A Hydrological Perspective*, Annual Review of Earth and Planetary Science **30** (2002) pp. 149-180. doi:10.1146/annurev.earth.30.091201.140434

6. E.G. Njoku and D. Entekhabi, *Passive Microwave Remote Sensing of Soil Moisture*, Journal of Hydrology **184** (1996) pp. 101-129. doi:10.1016/0022-1694(95)02970-2

7. M. Kodama, *Continuous Monitoring of Snow Water Equivalent Using Cosmic Ray Neutrons*, Cold Regions Science and Technology, **3** (1980) pp. 295-303. doi:10.1016/0165-232X(80)90036-1

8. M. Zreda, D. Desilets, T.P.A. Ferre and R.L. Scott, *Measuring Soil Moisture Content Non-Invasively at Intermediate Spatial Scale Using Cosmic-Ray Neutrons*, Geophysical Research Letters **35** (2008) L21402. doi:10.1029/2008GL035655

9. D. Desilets, M. Zreda and T. Ferre, *Nature's Neutron Probe: Land-Surface Hydrology at an Elusive Scale with Cosmic Rays*. Water Resources Research **46** (2010) W11505. doi:10.1029/2009WR008726

10. COSMOS [Online] http://cosmos.hwr.arizona.edu/

11. US News and World Report, "Cosmic Rays Detect Soil Moisture" http://www.usnews.com/mobile/articles_mobile/cosmic-rays-detect-soil-moisture

12. K. Nakamura *et al*. (Particle Data Group), Journal of Physics **G37** (2010) 075021.

13. T.K. Gaisser, *Cosmic Rays and Particle Physics*, Cambridge University Press, Cambridge, UK (1990) ISBN-9780521339315.

14. W.N. Hess, H.W. Patterson, R. Wallace, and E.L. Chupp, Physical Review **116** (1959) pp. 445-457. doi:10.1103/PhysRev.116.445

15. J.F. Ziegler, *Terrestrial Cosmic Rays*, IBM Journal of Research and Development **40** (1996) pp, 19-39. doi:10.1147/rd401.0019

16. R.J. Sheu, J.S. Lin, and S.H. Jiang, *A Study of the Cosmic-Ray Neutron Field Near Interfaces*, Nuclear Instruments and Methods **A476** (2001) pp. 74-79. doi:10.1016/S0168-9002(01)01395-X

17. N. Mascarenhas, *et al*., Development of a Neutron Scatter Camera for Fission Neutrons, IEEE Nuclear Science Symposium Conference Record (2006), San Diego, CA. doi:10.1109/NSSMIC.2006.356135

18. D. Desilets, N. Mascarenhas, P. Marleau and J. Brennan, *Land-Surface Hydrology with a Directional Neutron Detector (U)*, SAND2009-6321, Sandia National Laboratories, Albuquerque, NM (SRD), September 2009.

19. M.S. Gordon, *et al*., *Measurement of the Flux and Energy Spectrum of Cosmic-Ray Induced Neutrons on the Ground*, IEEE Transactions on Nuclear Science **51** (2004) pp. 3427-3434. doi:10.1109/TNS.2004.839134

20. L. Wielopolski, *et al*., *Basic Considerations for Monte Carlo Calculations in Soil*, Applied Radiation and Isotopes **62** (2005) pp. 97-107. doi:10.1016/j.apradiso.2004.06.003

21. O. Doron, L. Wielopolski, and S. Biegalski, Advantages of Mesh Tallying in MCNP5 for Soil Analysis Calculations, Journal of Radioanalytical and Nuclear Chemistry, v276 (2008) p183-186. doi:10.1007/s10967-007-0430-8

22. MCNP5 [Online] http://mcnp-green.lanl.gov/index.html

23. MCNP-X [Online] http://mcnpx.lanl.gov/

24. S.A. Pozzi, E. Padovani, and M. Marseguerra, *MCNP-PoliMi: A Monte-Carlo Code for Correlation Measurements*, Nuclear Instruments and Methods **A513** (2003) pp. 550-558. doi:10.1016/j.nima.2003.06.012

25. Eljen Technology, Sweetwater, TX 79556 [Online] http://www.eljentechnology.com/index.php

26. M.J. Berger, J.S. Coursey, M.A. Zucker, and J. Change, *Stopping-Power and Range Tables for Electrons, Protons, and Helium Ions*, [Online] http://www.nist.gov/pml/data/star/index.cfm

27. A. Enqvist, K. Weinfurther, M. Flaska and S.A. Pozzi, *Optimization of a Mixed Multiplicity Counter Using Monte Carlo Simulations and Measurements*, Conference Record IEEE NSS-MIC, Knoxville, TN. 2010.

28. Mesytec GmbH & Co. KG, 85640 Putzbrunn, Germany [Online] http://www.mesytec.com/

29. G. Dietz and H. Klein, *Gamma-Calibration of NE213 Scintillation Counters*, Nuclear Instruments and Methods **193** (1982) pp. 549-556. doi:10.1016/0029-554X(82)90249-X

30. ISO 8529-1 (2001) *Reference Neutron Radiations - Part 1: Characteristics and Methods of Production*.

31. L.A. Shepp and Y. Vardi, *Maximum Likelihood Reconstruction for Emission Tomography*, IEEE Transactions on Medical Imaging **MI-1** (1982) pp. 113-122. doi:10.1109/TMI.1982.4307558

DISTRIBUTION

1	MS0123	D. Chavez, LDRD Office	1011
1	MS0899	Technical Library	9536 (electronic copy)
1	MS1146	P. Griffin	1384
1	MS6913	D. Desilets	6913
1	MS9004	J. Lund	8130
1	MS9004	P. Davies	8100
1	MS9402	J. Goldsmith	8131
1	MS9406	P. Marleau	8132

Sandia National Laboratories